J. Fluid Mech. (2016), *vol.* 809, *pp.* 726–774. © Cambridge University Press 2016
doi:10.1017/jfm.2016.677

The effect of uniform electric field on the cross-stream migration of a drop in plane Poiseuille flow

Shubhadeep Mandal[1], Aditya Bandopadhyay[2] and Suman Chakraborty[1,2,†]

[1]Department of Mechanical Engineering, Indian Institute of Technology Kharagpur, West Bengal 721302, India

[2]Advanced Technology Development Center, Indian Institute of Technology Kharagpur, West Bengal 721302, India

(Received 10 September 2015; revised 6 October 2016; accepted 18 October 2016; first published online 15 November 2016)

The effect of a uniform electric field on the motion of a drop in an unbounded plane Poiseuille flow is studied analytically. The drop and suspending media are considered to be Newtonian and leaky dielectric. We solve for the two-way coupled electric and flow fields analytically by using a double asymptotic expansion for small charge convection and small shape deformation. We obtain two important mechanisms of cross-stream migration of the drop: (i) shape deformation and (ii) charge convection. The second one is a new source of cross-stream migration of the drop in plane Poiseuille flow which is due to an asymmetric charge distribution on the drop surface. Our study reveals that charge convection can cause a spherical non-deformable drop to migrate in the cross-stream direction. The combined effect of charge convection and shape deformation significantly alters the drop velocity, drop trajectory and steady state transverse position of the drop. We predict that, depending on the orientation of the applied uniform electric field and the relevant drop/medium electrohydrodynamic parameters, the drop may migrate either towards the centreline of the flow or away from it. We obtain that the final steady state transverse position of the drop is independent of its initial transverse position in the flow field. Most interestingly, we show that the drop can settle in an off-centreline steady state transverse position. Two-dimensional numerical simulations are also performed to study the drop motion in the combined presence of plane Poiseuille flow and a tilted electric field. The drop trajectory and steady state transverse position of the drop obtained from numerical simulations are in qualitative agreement with the analytical results.

Key words: drops, drops and bubbles

1. Introduction

Drops play a central role in interdisciplinary microfluidic and nanofluidic research (Teh *et al.* 2008; Casadevall i Solvas & deMello 2011; Seemann *et al.* 2012). They form a convenient means for rapid analytic detection and screening of chemicals (Zheng, Tice & Ismagilov 2004; Zhu & Fang 2013), protein crystallization (Zhu *et al.* 2014), medium for cell/particle encapsulation (Bhagat *et al.* 2010), reagent mixing

†Email address for correspondence: suman@mech.iitkgp.ernet.in

(Bringer *et al.* 2004), and biological assays (Guo *et al.* 2012). Precise control and manipulation of drops is of the utmost importance for realizing optimal functionalities in these concerned applications. Towards this, the effective manipulation of drops by various means such as thermocapillary (Baroud *et al.* 2007; Basu & Gianchandani 2008), acoustic streaming (Franke *et al.* 2009; Ding *et al.* 2013), electric field (Ahn *et al.* 2006; Link *et al.* 2006) and magnetic field (Pamme 2012) are of great practical importance. The above processes typically involve low Reynolds numbers based on the drop size and velocity. The cross-stream migration of a non-deforming spherical drop with a clean fluid–fluid interface, solely due to such a creeping flow field, is not possible, since the governing equations and boundary conditions are linear in nature (Leal 2007; Hanna & Vlahovska 2010). This linearity satisfies symmetry under flow reversal (Leal 2007; Hanna & Vlahovska 2010; Mukherjee & Sarkar 2013). The various mechanisms which lead to cross-stream migration of a drop include (i) drop deformation in shear flow near a solid wall (Chaffey, Brenner & Mason 1965; Karnis & Mason 1967; Chan & Leal 1979), (ii) drop deformation in the presence of flow curvature (Haber & Hetsroni 1971; Wohl & Rubinow 1974; Chan & Leal 1979; Wang & Dimitrakopoulos 2011; Mandal, Bandopadhyay & Chakraborty 2015; Stan *et al.* 2011), (iii) fluid inertia (Mortazavi & Tryggvason 2000; Magnaudet 2003; Khalili & Mortazavi 2012; Chen *et al.* 2014) (iv) flow-induced surfactant redistribution on the drop surface (Hanna & Vlahovska 2010; Pak, Feng & Stone 2014), (v) interface viscoelasticity (Schwalbe *et al.* 2011), (vi) fluid viscoelasticity (Chan & Leal 1979; Mukherjee & Sarkar 2013, 2014) etc. The underpinning nonlinearity in either the boundary conditions or the governing equations is the common tie between the aforementioned mechanisms which breaks the reversibility of the flow and causes cross-stream migration of drops. Previous studies have revealed several interesting aspects of drop dynamics in the presence of flow curvature, which is the focus of the present work. Chan & Leal (1979) have shown the pivotal role of flow curvature towards dictating the cross-stream migration of a deformable drop. They have shown that, depending on the viscosity of the drop and suspending medium, the drop may migrate either towards the centre of the Poiseuille flow or away from it. In two recent studies, Hanna & Vlahovska (2010) and Pak *et al.* (2014) have shown the non-trivial effect of surfactants at the drop surface which leads to cross-stream migration of a spherical drop towards the centre of the imposed Poiseuille flow.

The ease of integration and flexibility of operation renders an external electric field as a convenient means for drop manipulation in modern microfluidic devices. Studies on the response of drops towards an externally applied electric field have been carried out since the seminal work of Taylor (1966). Taylor (1966) introduced the leaky dielectric model, which considers small electrical conductivity of the liquids. Consideration of small electrical conductivity leads to the accumulation of charges at the drop interface. Taylor (1966) assumed that the interfacial charge distribution is solely governed by the Ohmic conduction. Since then, neglecting the convection of charges at the drop interface, several researchers have employed this model and studied the deformation of neutrally buoyant drops in the presence of uniform or non-uniform electric fields, and unbounded or bounded domains in an otherwise quiescent medium (Torza, Cox & Mason 1971; Im & Kang 2003; Vizika & Saville 2006; Lac & Homsy 2007; Supeene, Koch & Bhattacharjee 2008; Thaokar 2012; Deshmukh & Thaokar 2013; Lanauze, Walker & Khair 2013; Mandal, Chaudhury & Chakraborty 2014; Mandal, Bandopadhyay & Chakraborty 2016*a*). Most of these studies considered one-way coupled electrohydrodynamics – the applied electric field affects the flow field via the generation of Maxwell stress at the fluid–fluid

interface, while the electric field remains unaffected by the flow field. The electric field and flow field are coupled by the surface charge convection (i.e. interfacial convection of charges due to fluid flow). The effect of surface charge convection on the deformation of a drop in the presence of a uniform electric field in an otherwise quiescent medium is analysed by several studies (Feng 1999; Lanauze, Walker & Khair 2015; Das & Saintillan 2016). Another way in which the electric field and flow field are coupled is through shape deformation of the drop. Shape deformation can take place due to electrical and/or hydrodynamic stress at the drop interface. Very recently, Mandal, Bandopadhyay & Chakraborty (2016*b*) have studied the combined effect of charge convection and shape deformation on the motion of a drop in a non-uniform electric field (Mandal *et al.* 2016*b*). However, there appears to be scant literature which considers the two-way coupled effect of an electric field and an externally imposed background flow field in the combined presence of charge convection and shape deformation towards dictating the motion and deformation of drops (Ha & Yang 2000*b*; Xu & Homsy 2006; Vlahovska 2011; Bandopadhyay *et al.* 2016; Yariv & Almog 2016). The presence of a background flow field has been shown to markedly alter the charge distribution on the drop surface, which further alters the drop motion and deformation. Xu & Homsy (2006) considered the sedimentation of a non-neutrally buoyant drop in the presence of an axial uniform electric field. They concluded that the effect of charge convection has a profound impact on the settling velocity of the drop. Bandopadhyay *et al.* (2016) extended this study to include the effect of a tilted electric field on the sedimentation of the drop, and found lateral migration of the drop due to charge convection and shape deformation. Very recently, Yariv & Almog (2016) have obtained the effect of surface charge convection on drop sedimentation considering weak applied electric field. The effect of background linear flow in the presence of a uniform electric field on the deformation and orientation of drops has been studied both experimentally (Ha & Yang 2000*b*) and theoretically (Fernández 2008, 2009; Mahlmann & Papageorgiou 2009; Vlahovska 2011). Ha & Yang (2000*b*) have performed experiments on the effect of a uniform electric field on the rheological behaviour of a suspension of drops in shear flow and obtained that, depending on the relative strength of electric field and shear flow, the apparent viscosity of the suspension may increase or decrease. In a recent study, Vlahovska (2011) has performed a perturbation analysis to study the drop deformation, orientation characteristics and shear rheology of highly viscous drops in a uniform electric field in the presence of background linear flows. This study shows the pivotal role of shape deformation and charge convection on the rotation rate of the drop, effective shear viscosity and normal stress difference.

In many practical scenarios, suspended drops are transported by the application of a pressure gradient using syringe pumps. In such situations, it is quite expected that the drops encounter flow curvature. Despite the importance of flow curvature, there is no study present in the literature to the best of our knowledge which considers the effect of an external electric field on the drop motion in the presence of flow curvature. Motivated by this consideration, here we analyse the non-trivial implication of the curvature of the background plane Poiseuille flow field in the presence of a uniform electric field on a neutrally buoyant, Newtonian, leaky dielectric drop suspended in another immiscible Newtonian, leaky dielectric medium. Our results emphasize that the combined effect of uniform electric field and plane Poiseuille flow on the drop velocity is not a mere linear combination of drop velocities obtained in electric field and plane Poiseuille flow separately. This is due to the coupling between the electric potential and flow fields – the background flow field alters the distribution of charges

due to fluid flow at the drop surface, whereas the applied electric field alters the fluid flow via the generation of Maxwell stress at the drop interface. Considering the electric Reynolds number Re_E (given by the ratio of the charge-relaxation time scale to the convective time scale) and capillary number Ca (which signifies the relative strength of viscous stress as compared with surface tension or capillary stress) as the perturbation parameters, we arrive at analytical expressions for the drop velocity. Our major finding in the present study is that application of a uniform electric field not only alters the axial velocity of the drop but also dramatically affects the nature of the cross-stream migration of the drop. We identify two important mechanisms of cross-stream migration velocity: (i) shape deformation and (ii) charge convection. The presence of a tilted electric field makes the drop shape asymmetric with respect to the flow centreline, which leads to shape-deformation-induced cross-stream motion of the drop. Charge-convection-induced cross-stream migration is due to the asymmetric charge distribution on the drop surface. This component of cross-stream migration is present also for a non-deformable spherical drop. The combined effect of charge convection and shape deformation leads to cross-stream motion of a drop towards or away from the centreline of the imposed flow. In sharp contrast to the case of plane Poiseuille flow without any electric field, the presence of a tilted electric field leads to settling of the drop not only at the centreline but also below/above the centreline, depending on the orientation of the applied uniform electric field, the magnitude of the pertinent electrohydrodynamic property ratios of the drop and medium, and the associated non-dimensional numbers. Most surprisingly, the combined effect of a tilted uniform electric field and plane Poiseuille flow may lead to motion of a drop away from the centreline of the flow even if the drop is initially placed at the centreline of the flow. To validate these non-intuitive analytical results, we perform two-dimensional numerical simulations. The numerically obtained drop trajectory compares qualitatively with the analytical solution.

2. Problem formulation

We consider the motion of a drop of radius a in an unbounded domain in the presence of an imposed plane Poiseuille velocity field ($\boldsymbol{V}_\infty$) and a uniform electric field ($\boldsymbol{E}_\infty$). Plane Poiseuille flow is expressed in terms of a Cartesian coordinate system considering the drop centroid as origin in the following form: $\boldsymbol{V}_\infty = V_c(k_0 + k_1 x + k_2 x^2)\boldsymbol{e}_z$, where $k_0 = 4(x_d/H)(1 - x_d/H)$, $k_1 = (4/H)(1 - 2x_d/H)$ and $k_2 = -4/H^2$. This choice of imposed velocity field represents a pressure-driven flow between two parallel plates (infinite in the y and z directions) which are distance H apart in the transverse direction (x-direction). Here x_d is the transverse position of the drop centroid measured from the bottom wall. The imposed electric field is of the form $\boldsymbol{E}_\infty = E_c(E_x\boldsymbol{e}_x + E_z\boldsymbol{e}_z)$ with $E_x^2 + E_z^2 = 1$. Here V_c and E_c are the characteristic velocity and characteristic electric field, respectively. The imposed velocity acts in the z-direction (termed as axial direction), whereas the direction of the applied electric field can be altered by specifying the components of the imposed electric field along the axial (E_z) and transverse (E_x) directions. The drop liquid is considered to be Newtonian with a viscosity μ_i, density ρ_i, and leaky dielectric with an electrical conductivity σ_i and permittivity ε_i. The suspending fluid is also considered as Newtonian and leaky dielectric, with the hydrodynamic and electrical properties represented by the same symbols, except using the subscript 'e'. The drop interface is clean and the surface tension γ is constant. The spherical coordinate system (r, θ, ϕ) is attached at the centroid of the drop and moves with the drop at a velocity $\boldsymbol{U}_d$ which is yet to be determined (refer to figure 1). Here, we assume that

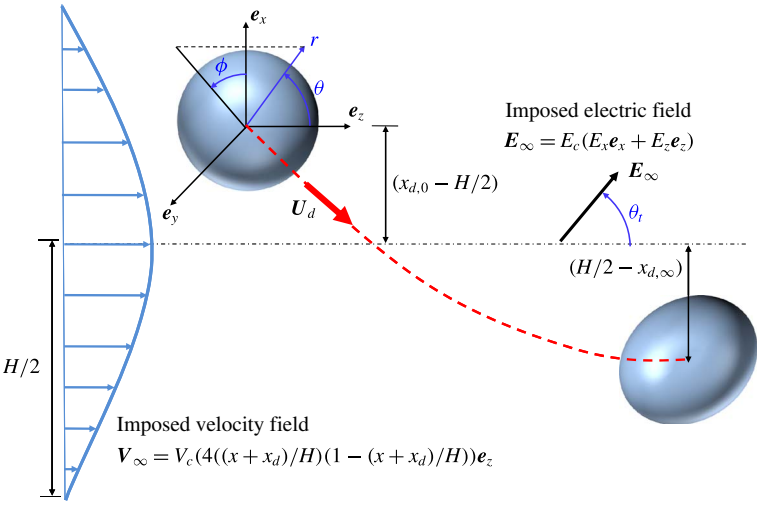

FIGURE 1. (Colour online) Schematic of a typical drop trajectory (dashed path) in an imposed plane Poiseuille flow field $\boldsymbol{V}_\infty$ in the presence of an imposed uniform electric field $\boldsymbol{E}_\infty$. A spherical coordinate system (r, θ, ϕ) is considered which is attached to the drop centroid. The velocity field is imposed in the axial direction (z-direction), whereas the imposed electric field is tilted at an angle θ_t (termed as tilt angle) with respect to the axial direction. Initially, the drop is placed at a transverse position $x_{d,0}$ and eventually the drop settles to some other transverse position $x_{d,\infty}$, at steady state. Transverse positions are measured from the bottom wall.

the Reynolds number based on drop radius (i.e. $Re = \rho_e V_c a/\mu_e$) is very small so that the fluid inertia is completely negligible (Chan & Leal 1979; Pak *et al.* 2014). We consider the drop as neutrally buoyant (i.e. $\rho_i = \rho_e$) so that gravity has no effect on the motion of the drop.

We non-dimensionalize length by the radius of the spherical drop a while the velocity scale is taken as V_c. The characteristic viscous stresses and electrical stresses are taken as $\tau_c^H = \mu_e V_c/a$ and $\tau_c^E = \varepsilon_e E_c^2$, respectively. Here we consider the properties of the external liquid as the characteristic quantities which yield the following property ratios (Bandopadhyay *et al.* 2016): viscosity ratio $\lambda = \mu_i/\mu_e$, conductivity ratio $R = \sigma_i/\sigma_e$ and permittivity ratio $S = \varepsilon_i/\varepsilon_e$. Using this non-dimensional scheme we obtain the following important non-dimensional numbers: capillary number $Ca = \mu_e V_c/\gamma$, electric Reynolds number $Re_E = \varepsilon_e V_c/a\sigma_e$ and Mason number $M = a\varepsilon_e E_c^2/\mu_e V_c$. The capillary number signifies the relative strength of the viscous stress in deforming the drop as compared with the force due to surface tension which resists the shape deformation. The electric Reynolds number signifies the relative importance of the charge-relaxation time scale as compared with the charge-convection time scale, whereas the Mason number signifies the relative importance of the electrical stress as compared with the viscous stress. Henceforth, all quantities will be represented non-dimensionally.

2.1. *Governing equations and boundary conditions*

The drop and the suspending medium are considered as weakly conducting liquids under the paradigm of the leaky dielectric model (Taylor 1966; Melcher & Taylor 1969; Saville 1997). The leaky dielectric model assumes the bulk liquids as charge-free, and the mismatch between the conductivity and permittivity of the two liquids

manifests in terms of the interfacial charge at the drop surface only. Hence, the electric potentials inside and outside the drop ($\psi_{i,e}$) satisfy the Laplace equation

$$\left.\begin{aligned}\nabla^2\psi_i &= 0,\\ \nabla^2\psi_e &= 0.\end{aligned}\right\} \tag{2.1}$$

The electric potentials inside and outside the drop satisfy the following boundary conditions (Bandopadhyay *et al.* 2016):

($e1$) the electric potential inside the drop ψ_i is bounded at the origin of the spherical coordinate system;

($e2$) the electric potential outside the drop ψ_e approaches the specified potential at infinity, ψ_∞, which is given in terms of the electric field as: $\boldsymbol{\nabla}\psi_\infty = -\boldsymbol{E}_\infty$;

($e3$) the electric potential is continuous at the surface of the drop: at $r = r_s$, $\psi_i = \psi_e$;

($e4$) the charges present at the drop surface satisfy the following conservation equation: at $r = r_s$, $\boldsymbol{n}\cdot(R\boldsymbol{\nabla}\psi_i - \boldsymbol{\nabla}\psi_e) = -Re_E\boldsymbol{\nabla}_s\cdot(q_s\boldsymbol{V}_s)$, where q_s is the surface charge given as $q_s = \boldsymbol{n}\cdot(S\boldsymbol{\nabla}\psi_i - \boldsymbol{\nabla}\psi_e)|_{r=r_s}$, $\boldsymbol{V}_s$ is the fluid velocity at the drop surface and $\boldsymbol{\nabla}_s = [\boldsymbol{\nabla} - \boldsymbol{n}(\boldsymbol{n}\cdot\boldsymbol{\nabla})]$ represents the surface divergence operator. One thing to note here is that the drop surface r_s is given by $r_s = 1 + f(\theta,\phi)$, where $f(\theta,\phi)$ represents the deviation of the drop shape from sphericity. The outward unit normal vector $\boldsymbol{n}$ is related to the drop shape through $\boldsymbol{n} = \boldsymbol{\nabla}(r - r_s)/|\boldsymbol{\nabla}(r - r_s)|$. It is important to note that the fourth boundary condition ($e4$) is valid under the quasi-steady-state approximation in which the surface charges adjust to the background spatially varying flow field instantaneously.

Under the quasi-steady-state approximation, the velocity and pressure fields inside and outside the drop ($\boldsymbol{u}_{i,e}$, $p_{i,e}$) satisfy the Stokes equation and the condition of incompressibility of the form

$$\left.\begin{aligned}\boldsymbol{\nabla}p_i &= \lambda\nabla^2\boldsymbol{u}_i, \quad \boldsymbol{\nabla}\cdot\boldsymbol{u}_i = 0,\\ \boldsymbol{\nabla}p_e &= \nabla^2\boldsymbol{u}_e, \quad \boldsymbol{\nabla}\cdot\boldsymbol{u}_e = 0,\end{aligned}\right\} \tag{2.2}$$

where ($\boldsymbol{u}_i$, p_i) and ($\boldsymbol{u}_e$, p_e) represent the velocity and the pressure fields inside and outside the drop, respectively.

The flow fields inside and outside the drop satisfy the following boundary conditions (Bandopadhyay *et al.* 2016):

($f1$) the velocity ($\boldsymbol{u}_i$) and pressure (p_i) inside the drop are bounded at the origin of the spherical coordinate system;

($f2$) the velocity outside the drop, $\boldsymbol{u}_e$, approaches the specified imposed plane Poiseuille flow velocity at infinity, which in a reference frame attached to the drop centroid (moving at a velocity of $\boldsymbol{U}_d$) is given by: $\boldsymbol{u}_e|_{r\to\infty} = \boldsymbol{V}_\infty - \boldsymbol{U}_d$;

($f3$) the velocity is continuous at the drop surface, and at steady state the normal component of the velocity at the drop surface is zero: at $r = r_s$, $\boldsymbol{u}_i = \boldsymbol{u}_e$ and $\boldsymbol{u}_i\cdot\boldsymbol{n} = \boldsymbol{u}_e\cdot\boldsymbol{n} = 0$;

($f4$) the tangential component of the total stress (hydrodynamic and electrical Maxwell stresses) is continuous at the drop surface: at $r = r_s$, $\boldsymbol{n}\cdot\boldsymbol{\tau}_i\cdot(\boldsymbol{I} - \boldsymbol{nn}) = \boldsymbol{n}\cdot\boldsymbol{\tau}_e\cdot(\boldsymbol{I} - \boldsymbol{nn})$;

($f5$) the normal component of the total stress is balanced by the capillary stress at the drop surface: at $r = r_s$, $\boldsymbol{n}\cdot\boldsymbol{\tau}_e\cdot\boldsymbol{n} - \boldsymbol{n}\cdot\boldsymbol{\tau}_i\cdot\boldsymbol{n} = (1/Ca)(\boldsymbol{\nabla}\cdot\boldsymbol{n})$,

where $\boldsymbol{\tau}_{i,e}$ is the total stress tensor with contributions from hydrodynamic and electrical effects, and $\boldsymbol{I}-\boldsymbol{nn}$ represents the surface projection operator. The total stress tensor is given by $\boldsymbol{\tau}_{i,e}=\boldsymbol{\tau}_{i,e}^{H}+M\boldsymbol{\tau}_{i,e}^{E}$, where $\boldsymbol{\tau}_{i,e}^{H}$ is the viscous stress tensor and $\boldsymbol{\tau}_{i,e}^{E}$ is the electrical Maxwell stress tensor of the following form

$$\left.\begin{aligned} \boldsymbol{\tau}_{i}^{H}&=[-p_i\boldsymbol{I}+\lambda\{\boldsymbol{\nabla u}_i+(\boldsymbol{\nabla u}_i)^{\mathrm{T}}\}], \quad \boldsymbol{\tau}_{e}^{H}=[-p_e\boldsymbol{I}+\{\boldsymbol{\nabla u}_e+(\boldsymbol{\nabla u}_e)^{\mathrm{T}}\}],\\ \boldsymbol{\tau}_{i}^{E}&=S\left[\boldsymbol{E}_i(\boldsymbol{E}_i)^{\mathrm{T}}-\tfrac{1}{2}|\boldsymbol{E}_i|^2\boldsymbol{I}\right], \quad \boldsymbol{\tau}_{e}^{E}=\left[\boldsymbol{E}_e(\boldsymbol{E}_e)^{\mathrm{T}}-\tfrac{1}{2}|\boldsymbol{E}_e|^2\boldsymbol{I}\right]. \end{aligned}\right\} \tag{2.3}$$

2.2. *Expansion in perturbation of Re_E and Ca*

One important thing to note here is that the analytical solution of the present electrohydrodynamic problem is not straightforward, due to the nonlinearity associated with the charge convection (see boundary condition $e4$) at the drop surface even in the limit of a non-deforming spherical drop (Feng 1999; Vlahovska 2011). Another nonlinearity which is commonly present in problems having a fluid–fluid interface is associated with the unknown shape of the interface (Leal 2007; Mandal, Ghosh & Chakraborty 2016). In the present problem the drop shape is not known *a priori*, but the drop shape should be known beforehand to implement the boundary conditions at the drop interface. Towards further analytical development, we first identify different physical systems depending on the relative magnitude of the dimensionless numbers (Re_E, Ca and M). System with Re_E, $Ca\ll 1$, $M\sim 1$: physical systems of this kind can be solved analytically by considering the electric Reynolds number Re_E and the capillary number Ca as the perturbation parameters (Xu & Homsy 2006). A typical example of this kind of droplet-based microfluidic system is one in which a silicone oil (with $\rho_i=970$ kg m^{-3}, $\varepsilon_i=2.65\varepsilon_0$, $\sigma_i=0.8\times10^{-12}$ S m^{-1}, $\mu_i=0.34$ Pa s, where ε_0 is permittivity of free space) drop of radius $a=4$ mm is suspended in castor oil (with $\rho_e=960$ kg m^{-3}, $\varepsilon_e=4.7\varepsilon_0$, $\sigma_e=4\times10^{-11}$ S m^{-1}, $\mu_e=0.78$ Pa s) (Mhatre & Thaokar 2013). In the presence of a uniform electric field of strength $E_c=10^5$ V m^{-1}, background Poiseuille flow of centreline velocity $V_c=1$ mm s^{-1} and surface tension $\gamma=4\times10^{-3}$ N m^{-1}, we obtain the dimensionless numbers as $Re_E=0.26$, $Ca=0.2$ and $M=2.1$. System with $M\ll 1$, $Re_E\sim 1$: this kind of system for the case of settling of drop in uniform electric field has been solved analytically considering M as the perturbation parameter by Yariv & Almog (2016) and is valid even for $Ca\sim 1$. System with $Ca\ll 1$, Re_E, $M\sim 1$: this kind of system can be solved analytically considering Ca as the perturbation parameter. Very recently, Das & Saintillan (2016) have obtained drop deformation in this limit semi-analytically. Here we focus on the solution of the physical systems of the first kind by employing a double asymptotic expansion considering $1\gg Re_E$, $Ca\gg Re_E^2$, Re_ECa, Ca^2 and $M\sim 1$. Thus we seek a regular domain perturbation solution for the electric potential, velocity, pressure and stress fields of the following form

$$\left.\begin{aligned} \psi_{i,e}&=\psi_{i,e}^{(0)}+Re_E\psi_{i,e}^{(Re_E)}+Ca\psi_{i,e}^{(Ca)}+\cdots,\\ \boldsymbol{u}_{i,e}&=\boldsymbol{u}_{i,e}^{(0)}+Re_E\boldsymbol{u}_{i,e}^{(Re_E)}+Ca\boldsymbol{u}_{i,e}^{(Ca)}+\cdots,\\ p_i&=\frac{1}{Ca}p_i^{(1/Ca)}+p_i^{(0)}+Re_Ep_i^{(Re_E)}+Cap_i^{(Ca)}+\cdots,\\ p_e&=p_e^{(0)}+Re_Ep_e^{(Re_E)}+Cap_e^{(Ca)}+\cdots,\\ \boldsymbol{\tau}_i&=\frac{1}{Ca}\boldsymbol{\tau}_i^{(1/Ca)}+\boldsymbol{\tau}_i^{(0)}+Re_E\boldsymbol{\tau}_i^{(Re_E)}+Ca\boldsymbol{\tau}_i^{(Ca)}+\cdots,\\ \boldsymbol{\tau}_e&=\boldsymbol{\tau}_e^{(0)}+Re_E\boldsymbol{\tau}_e^{(Re_E)}+Ca\boldsymbol{\tau}_e^{(Ca)}+\cdots, \end{aligned}\right\} \tag{2.4}$$

where $p_i^{(1/Ca)}$ and $\boldsymbol{\tau}_i^{(1/Ca)}$ are required to balance the pressure jump across the drop in the absence of any flow field (Chan & Leal 1979).

The unknown drop velocity $\boldsymbol{U}_d$ is also expanded in the following form

$$\boldsymbol{U}_d = \boldsymbol{U}_d^{(0)} + Re_E \boldsymbol{U}_d^{(Re_E)} + Ca\boldsymbol{U}_d^{(Ca)} + \cdots, \tag{2.5}$$

where $\boldsymbol{U}_d^{(0)}$ is the leading-order drop velocity representing the drop velocity in the absence of charge convection and shape deformation, $\boldsymbol{U}_d^{(Re_E)}$ denotes the first correction to drop velocity due to charge convection when the shape deformation is absent, and $\boldsymbol{U}_d^{(Ca)}$ denotes the first correction to drop velocity due to shape deformation when the charge convection is absent. At this order of approximation, the linear combination of these two effects gives the simultaneous effect of charge convection and shape deformation (refer to appendix A of Mandal *et al.* (2016*b*) for detail justification).

The unknown drop shape is also expanded in the following perturbation form (Bandopadhyay *et al.* 2016)

$$r_s = 1 + f(\theta, \phi) = 1 + Caf^{(Ca)} + Ca\,Re_E f^{(Ca\,Re_E)} + Ca^2 f^{(Ca^2)} + \cdots, \tag{2.6}$$

where $f^{(Ca)}$, $f^{(Ca\,Re_E)}$ and $f^{(Ca^2)}$ are the corrections in drop shape from sphericity. The outward unit normal ($\boldsymbol{n}$) and curvature of the drop interface ($\boldsymbol{\nabla}\cdot\boldsymbol{n}$) can be expressed in terms of the drop shape (Bandopadhyay *et al.* 2016).

The leading-order electric potentials inside and outside the drop ($\psi_{i,e}^{(0)}$) satisfy the Laplace equation of the form

$$\left.\begin{aligned} \nabla^2\psi_i^{(0)} &= 0, \\ \nabla^2\psi_e^{(0)} &= 0. \end{aligned}\right\} \tag{2.7}$$

The boundary conditions ($e1$–$e4$) at the leading order transform to the following:

$$\left.\begin{aligned} \psi_e^{(0)}|_{r\to\infty} &\to \psi_\infty, \\ \psi_i^{(0)} \text{ bounded for } r &< 1, \\ \psi_e^{(0)}|_{r=1} &= \psi_i^{(0)}|_{r=1}, \\ \boldsymbol{e}_r\cdot(R\boldsymbol{\nabla}\psi_i^{(0)} - \boldsymbol{\nabla}\psi_e^{(0)})|_{r=1} &= 0, \end{aligned}\right\} \tag{2.8}$$

where the generic notation $\xi|_{r=1}$ is used to denote that the quantity ξ is evaluated at $r=1$.

The leading-order inner and outer flow fields ($\boldsymbol{u}_{i,e}^{(0)}, p_{i,e}^{(0)}$) satisfy the Stokes equation and the condition of incompressibility of the form

$$\left.\begin{aligned} \boldsymbol{\nabla}p_i^{(0)} &= \lambda\nabla^2\boldsymbol{u}_i^{(0)}, \quad \boldsymbol{\nabla}\cdot\boldsymbol{u}_i^{(0)} = 0, \\ \boldsymbol{\nabla}p_e^{(0)} &= \nabla^2\boldsymbol{u}_e^{(0)}, \quad \boldsymbol{\nabla}\cdot\boldsymbol{u}_e^{(0)} = 0. \end{aligned}\right\} \tag{2.9}$$

The boundary conditions ($f1$–$f4$) at the leading order are

$$\left.\begin{aligned} \boldsymbol{u}_e^{(0)}|_{r\to\infty} &\to (\boldsymbol{V}_\infty^{(0)} - \boldsymbol{U}_d^{(0)}), \\ \boldsymbol{u}_i^{(0)} \text{ is bounded for } r &< 1, \\ \boldsymbol{u}_e^{(0)}|_{r=1} &= \boldsymbol{u}_i^{(0)}|_{r=1}, \\ \boldsymbol{u}_e^{(0)}|_{r=1}\cdot\boldsymbol{e}_r &= \boldsymbol{u}_i^{(0)}|_{r=1}\cdot\boldsymbol{e}_r = 0, \\ \boldsymbol{e}_r\cdot(\boldsymbol{\tau}_e^{(0)} - \boldsymbol{\tau}_i^{(0)})|_{r=1}\cdot(\boldsymbol{I} - \boldsymbol{e}_r\boldsymbol{e}_r) &= 0, \\ \boldsymbol{e}_r\cdot(\boldsymbol{\tau}_e^{(0)} - \boldsymbol{\tau}_i^{(0)})|_{r=1}\cdot\boldsymbol{e}_r &= -(2f^{(Ca)} + \nabla^2 f^{(Ca)}). \end{aligned}\right\} \tag{2.10}$$

At $O(Re_E)$, which brings the first effect of charge convection, the electric potentials inside and outside the drop ($\psi_{i,e}^{(Re_E)}$) satisfy the Laplace equation of the form

$$\left.\begin{aligned}\nabla^2\psi_i^{(Re_E)} &= 0,\\ \nabla^2\psi_e^{(Re_E)} &= 0.\end{aligned}\right\} \tag{2.11}$$

Quite naturally, the boundary conditions for electric potential at this order are not the same as that of the leading order. At $O(Re_E)$ the effect of charge convection plays a big role in determining the electric potential distribution. The boundary conditions ($e1$–$e4$) take the following form

$$\left.\begin{aligned}\psi_e^{(Re_E)}|_{r\to\infty} &\to 0,\\ \psi_i^{(Re_E)} \text{ bounded for } r &< 1,\\ \psi_i^{(Re_E)}|_{r=1} &= \psi_e^{(Re_E)}|_{r=1},\\ \boldsymbol{e}_r\cdot(R\nabla\psi_i^{(Re_E)} - \nabla\psi_e^{(Re_E)})|_{r=1} &= -\{\nabla_s\cdot(q_s^{(0)}\boldsymbol{V}_s^{(0)})\}|_{r=1},\end{aligned}\right\} \tag{2.12}$$

where the surface charge distribution of the leading order is given by $q_s^{(0)} = \boldsymbol{e}_r\cdot(S\nabla\psi_i^{(0)} - \nabla\psi_e^{(0)})|_{r=1}$, and the velocity at the drop surface $\boldsymbol{V}_s^{(0)} = \boldsymbol{u}_i^{(0)}|_{r=1}$.

At $O(Re_E)$, the velocity and pressure fields inside and outside the drop ($\boldsymbol{u}_{i,e}^{(Re_E)}, p_{i,e}^{(Re_E)}$) satisfy the Stokes equation and the condition of incompressibility of the form

$$\left.\begin{aligned}\nabla p_i^{(Re_E)} &= \lambda\nabla^2\boldsymbol{u}_i^{(Re_E)}, \quad \nabla\cdot\boldsymbol{u}_i^{(Re_E)} = 0,\\ \nabla p_e^{(Re_E)} &= \nabla^2\boldsymbol{u}_e^{(Re_E)}, \quad \nabla\cdot\boldsymbol{u}_e^{(Re_E)} = 0,\end{aligned}\right\} \tag{2.13}$$

which are subject to the following boundary conditions

$$\left.\begin{aligned}\boldsymbol{u}_e^{(Re_E)}|_{r\to\infty} &\to (-\boldsymbol{U}_d^{(Re_E)}),\\ \boldsymbol{u}_i^{(Re_E)} \text{ is bounded for } r &< 1,\\ \boldsymbol{u}_e^{(Re_E)}|_{r=1} &= \boldsymbol{u}_i^{(Re_E)}|_{r=1},\\ \boldsymbol{u}_e^{(Re_E)}|_{r=1}\cdot\boldsymbol{e}_r &= \boldsymbol{u}_i^{(Re_E)}|_{r=1}\cdot\boldsymbol{e}_r = 0,\\ \boldsymbol{e}_r\cdot(\boldsymbol{\tau}_e^{(Re_E)} - \boldsymbol{\tau}_i^{(Re_E)})|_{r=1}\cdot(\boldsymbol{I} - \boldsymbol{e}_r\boldsymbol{e}_r) &= 0,\\ \boldsymbol{e}_r\cdot(\boldsymbol{\tau}_e^{(Re_E)} - \boldsymbol{\tau}_i^{(Re_E)})|_{r=1}\cdot\boldsymbol{e}_r &= -(2f^{(Ca\,Re_E)} + \nabla^2 f^{(Ca\,Re_E)}).\end{aligned}\right\} \tag{2.14}$$

At $O(Ca)$, which brings the effect of shape deformation, the electric potentials inside and outside the drop ($\psi_{i,e}^{(Ca)}$) satisfy the Laplace equation of the form

$$\left.\begin{aligned}\nabla^2\psi_i^{(Ca)} &= 0,\\ \nabla^2\psi_e^{(Ca)} &= 0,\end{aligned}\right\} \tag{2.15}$$

which are subject to the following boundary conditions

$$\left.\begin{aligned}\psi_e^{(Ca)}|_{r\to\infty} &\to 0,\\ \psi_i^{(Ca)} \text{ bounded for } r &< 1,\\ [\psi_e|_{r=1+Caf^{(Ca)}}]^{(Ca)} &= [\psi_i|_{r=1+Caf^{(Ca)}}]^{(Ca)},\\ [\boldsymbol{n}\cdot(R\nabla\psi_i - \nabla\psi_e)|_{r=1+Caf^{(Ca)}}]^{(Ca)} &= 0,\end{aligned}\right\} \tag{2.16}$$

where the generic representation $[\xi|_{r=1+Caf^{(Ca)}}]^{(Ca)}$ is used to denote the $O(Ca)$ contribution of any quantity ξ of the following form (Brenner 1964)

$$[\xi|_{r=1+Caf^{(Ca)}}]^{(Ca)} = \left(\xi^{(Ca)}|_{r=1} + f^{(Ca)}\left.\frac{\partial \xi^{(0)}}{\partial r}\right|_{r=1}\right), \tag{2.17}$$

where we have evaluated the quantity ξ at the deformed drop interface $r = 1 + Caf^{(Ca)}$ by using Taylor series expansion around the spherical drop interface ($r = 1$).

The $O(Ca)$ velocity and pressure fields inside and outside the drop $(\boldsymbol{u}_{i,e}^{(Ca)}, p_{i,e}^{(Ca)})$ satisfy the Stokes equation and the condition of incompressibility of the following form

$$\left.\begin{aligned} \nabla p_i^{(Ca)} &= \lambda \nabla^2 \boldsymbol{u}_i^{(Ca)}, \quad \nabla \cdot \boldsymbol{u}_i^{(Ca)} = 0, \\ \nabla p_e^{(Ca)} &= \nabla^2 \boldsymbol{u}_e^{(Ca)}, \quad \nabla \cdot \boldsymbol{u}_e^{(Ca)} = 0, \end{aligned}\right\} \tag{2.18}$$

which are subject to the following boundary conditions

$$\left.\begin{aligned} \boldsymbol{u}_e^{(Ca)}|_{r\to\infty} &\to (-\boldsymbol{U}_d^{(Ca)}), \\ \boldsymbol{u}_i^{(Ca)} &\text{ is bounded for } r < 1, \\ [\boldsymbol{u}_e|_{r=1+Caf^{(Ca)}}]^{(Ca)} &= [\boldsymbol{u}_i|_{r=1+Caf^{(Ca)}}]^{(Ca)}, \\ [\boldsymbol{u}_e|_{r=1+Caf^{(Ca)}} \cdot \boldsymbol{n}]^{(Ca)} &= [\boldsymbol{u}_i|_{r=1+Caf^{(Ca)}} \cdot \boldsymbol{n}]^{(Ca)} = 0, \\ [\boldsymbol{n} \cdot (\boldsymbol{\tau}_e - \boldsymbol{\tau}_i)|_{r=1+Caf^{(Ca)}} \cdot (\boldsymbol{I} - \boldsymbol{nn})]^{(Ca)} &= 0, \\ [\boldsymbol{n} \cdot (\boldsymbol{\tau}_e - \boldsymbol{\tau}_i)|_{r=1+Caf^{(Ca)}} \cdot \boldsymbol{n}]^{(Ca)} &= 2f^{(Ca)}(f^{(Ca)} + \nabla^2 f^{(Ca)}) - (2f^{(Ca^2)} + \nabla^2 f^{(Ca^2)}). \end{aligned}\right\} \tag{2.19}$$

3. Asymptotic solution for small charge convection and small shape deformation

3.1. *Description of electric potential, velocity and pressure fields*

Here we present the solution methodology to obtain the electric potential, velocity and pressure fields at different orders of perturbation. As the electric potentials inside and outside the drop satisfy the Laplace equation, we can represent the electric potentials as (Vlahovska 2011)

$$\left.\begin{aligned} \psi_i^{(j)} &= \sum_{n=0}^{\infty} r^n \sum_{m=0}^{n} [a_{n,m}^{(j)} \cos(m\phi) + \hat{a}_{n,m}^{(j)} \sin(m\phi)] P_{n,m}, \\ \psi_e^{(j)} &= \psi_\infty^{(j)} + \sum_{n=0}^{\infty} r^{-n-1} \sum_{m=0}^{n} [b_{-n-1,m}^{(j)} \cos(m\phi) + \hat{b}_{-n-1,m}^{(j)} \sin(m\phi)] P_{n,m}, \end{aligned}\right\} \tag{3.1}$$

where $P_{n,m}$ are the associated Legendre polynomials with argument $\cos\theta$, degree n and order m. In (3.1) we have used the superscript j to represent different orders of perturbation, which takes the following three forms $j = 0, Re_E, Ca$. One thing to note here is that as the electric potential inside the drop in bounded, the electric potential inside the drop $(\psi_i^{(j)})$ is represented by the growing spherical solid harmonics. On the other hand the electric potential outside the drop should match with the applied external electric potential at infinity, that is why the electric potential outside the drop $(\psi_e^{(j)})$ is represented by the unperturbed potential $\psi_\infty^{(j)}$ and decaying spherical solid harmonics. The unperturbed potential which is applied externally exists only at the leading order (i.e. $j = 0$) of the form $\psi_\infty^{(0)} = -r(E_x P_{1,1} \cos\phi + E_z P_{1,0})$. Now our

task is to determine the unknown coefficients ($a_{n,m}^{(j)}$, $\hat{a}_{n,m}^{(j)}$, $b_{-n-1,m}^{(j)}$ and $\hat{b}_{-n-1,m}^{(j)}$) which are present in the expressions of the electric potentials (3.1) by invoking appropriate boundary conditions, with proper use of the orthogonality property of the associated Legendre polynomials.

The velocity and pressure fields inside and outside the drop satisfy the Stokes equation and the condition of incompressibility at each order of perturbation. In spherical coordinates, the general solution of Stokes equation which satisfies the continuity equation is given by Lamb's general solution in terms of solid spherical harmonics (Lamb 1975). The velocity and pressure fields inside and outside the drop are given by (Hetsroni & Haber 1970; Happel & Brenner 1981)

$$\boldsymbol{u}_i^{(j)} = \sum_{n=1}^{\infty} \left[\nabla \times (\boldsymbol{r}\chi_n^{(j)}) + \nabla \Phi_n^{(j)} + \frac{n+3}{2(n+1)(2n+3)\lambda} r^2 \nabla p_n^{(j)} - \frac{n}{(n+1)(2n+3)\lambda} \boldsymbol{r} p_n^{(j)} \right], \tag{3.2}$$

$$p_i^{(j)} = \sum_{n=1}^{\infty} p_n^{(j)}, \tag{3.3}$$

$$\begin{aligned} \boldsymbol{u}_e^{(j)} \;=\; \boldsymbol{V}_{\infty}^{(j)} - \boldsymbol{U}_d^{(j)} + \boldsymbol{v}_e^{(j)} = \boldsymbol{V}_{\infty}^{(j)} - \boldsymbol{U}_d^{(j)} + \sum_{n=1}^{\infty} \Bigg[\nabla \times (\boldsymbol{r}\chi_{-n-1}^{(j)}) + \nabla \Phi_{-n-1}^{(j)} \\ - \frac{n-2}{2n(2n-1)} r^2 \nabla p_{-n-1}^{(j)} + \frac{n+1}{n(2n-1)} \boldsymbol{r} p_{-n-1}^{(j)} \Bigg], \end{aligned} \tag{3.4}$$

$$p_e^{(j)} = \sum_{n=1}^{\infty} p_{-n-1}^{(j)}. \tag{3.5}$$

The flow field inside the drop is represented in terms of growing solid spherical harmonics $p_n^{(j)}$, $\Phi_n^{(j)}$ and $\chi_n^{(j)}$ of the form (Bandopadhyay *et al.* 2016)

$$\left.\begin{aligned} p_n^{(j)} &= \lambda r^n \sum_{m=0}^{n} [A_{n,m}^{(j)} \cos(m\phi) + \hat{A}_{n,m}^{(j)} \sin(m\phi)] P_{n,m}, \\ \Phi_n^{(j)} &= r^n \sum_{m=0}^{n} [B_{n,m}^{(j)} \cos(m\phi) + \hat{B}_{n,m}^{(j)} \sin(m\phi)] P_{n,m}, \\ \chi_n^{(j)} &= r^n \sum_{m=0}^{n} [C_{n,m}^{(j)} \cos(m\phi) + \hat{C}_{n,m}^{(j)} \sin(m\phi)] P_{n,m}, \end{aligned}\right\} \tag{3.6}$$

whereas the flow field outside the drop is represented by the unperturbed velocity field ($\boldsymbol{V}_{\infty}^{(j)} - \boldsymbol{U}_d^{(j)}$) and the decaying field $\boldsymbol{v}_e^{(j)}$, which consists of the decaying solid spherical harmonics $p_{-n-1}^{(j)}$, $\Phi_{-n-1}^{(j)}$ and $\chi_{-n-1}^{(j)}$ of the form (Bandopadhyay *et al.* 2016)

$$\left.\begin{aligned} p_{-n-1}^{(j)} &= r^{-n-1} \sum_{m=0}^{n} [A_{-n-1,m}^{(j)} \cos(m\phi) + \hat{A}_{-n-1,m}^{(j)} \sin(m\phi)] P_{n,m}, \\ \Phi_{-n-1}^{(j)} &= r^{-n-1} \sum_{m=0}^{n} [B_{-n-1,m}^{(j)} \cos(m\phi) + \hat{B}_{-n-1,m}^{(j)} \sin(m\phi)] P_{n,m}, \\ \chi_{-n-1}^{(j)} &= r^{-n-1} \sum_{m=0}^{n} [C_{-n-1,m}^{(j)} \cos(m\phi) + \hat{C}_{-n-1,m}^{(j)} \sin(m\phi)] P_{n,m}. \end{aligned}\right\} \tag{3.7}$$

In (3.2) and (3.4), $\boldsymbol{r}$ represents the dimensionless position vector and $r = |\boldsymbol{r}|$ represents the magnitude of $\boldsymbol{r}$. Now our task is to determine the unknown coefficients present in the velocity and pressure fields $A_{n,m}^{(j)}$, $B_{n,m}^{(j)}$, $C_{n,m}^{(j)}$, $A_{-n-1,m}^{(j)}$, $B_{-n-1,m}^{(j)}$, $C_{-n-1,m}^{(j)}$, $\hat{A}_{n,m}^{(j)}$, $\hat{B}_{n,m}^{(j)}$, $\hat{C}_{n,m}^{(j)}$, $\hat{A}_{-n-1,m}^{(j)}$, $\hat{B}_{-n-1,m}^{(j)}$ and $C_{-n-1,m}^{(j)}$ by invoking proper boundary conditions at each order of perturbation. Our aim is to determine the drop velocity at each order of perturbation, with proper use of the orthogonality property of the surface harmonics. Towards this we use the velocity boundary conditions (except the condition of normal stress balance) to obtain the unknown coefficients present in the solid spherical harmonics (3.6) and (3.7). Then we apply the force-free condition to obtain the drop velocity $\boldsymbol{U}_d^{(j)}$. The shape of the drop can be determined by using the normal stress balance condition. This method has been previously used by several authors (Hetsroni & Haber 1970; Bandopadhyay *et al.* 2016) to obtain the drop velocity and shape.

3.2. *Leading-order solution*

The electric potential distribution at the leading order is obtained by substituting the electric potentials given in (3.1) in the boundary conditions (2.8). The leading-order electric potentials inside and outside the drop ($\psi_{i,e}^{(0)}$) are obtained as (Bandopadhyay *et al.* 2016)

$$\left.\begin{aligned}\psi_i^{(0)} &= -\left(\frac{3E_z}{2+R}\right) rP_{1,0} - \left(\frac{3E_x\cos\phi}{2+R}\right) rP_{1,1},\\ \psi_e^{(0)} &= -r(E_xP_{1,1}\cos\phi + E_zP_{1,0}) + \left(\frac{E_z(R-1)}{(2+R)}\right)\frac{1}{r^2}P_{1,0} + \left(\frac{E_x(R-1)\cos\phi}{2+R}\right)\frac{1}{r^2}P_{1,1}.\end{aligned}\right\} \tag{3.8}$$

Consequently, the leading-order surface charge distribution is obtained as $q_s^{(0)} = ((3(R-S))/(R+2))[E_zP_{1,0} + E_xP_{1,1}\cos\phi]$.

Proceeding further, the velocity and pressure fields inside and outside the drop in terms of spherical solid harmonics are substituted in (2.10) (first five boundary conditions) to obtain the leading-order flow field in the following form

$$\boldsymbol{u}_i^{(0)} = \left[\begin{array}{l}\nabla\times(\boldsymbol{r}\chi_1^{(0)} + \boldsymbol{r}\chi_2^{(0)}) + \nabla(\Phi_1^{(0)} + \Phi_2^{(0)} + \Phi_3^{(0)})\\ \quad + \dfrac{r^2}{\lambda}\left(\dfrac{1}{5}\nabla p_1^{(0)} + \dfrac{5}{42}\nabla p_2^{(0)} + \dfrac{1}{12}\nabla p_3^{(0)}\right) - \dfrac{\boldsymbol{r}}{\lambda}\left(\dfrac{1}{10}p_1^{(0)} + \dfrac{2}{21}p_2^{(0)} + \dfrac{1}{12}p_3^{(0)}\right)\end{array}\right], \tag{3.9}$$

$$p_i^{(0)} = p_1^{(0)} + p_2^{(0)} + p_3^{(0)}, \tag{3.10}$$

$$\boldsymbol{u}_e^{(0)} = \left[\begin{array}{l}\nabla\times(\boldsymbol{r}\chi_{-3}^{(0)}) + \nabla(\Phi_{-2}^{(0)} + \Phi_{-3}^{(0)} + \Phi_{-4}^{(0)}) + r^2\left(\frac{1}{2}\nabla p_{-2}^{(0)} - \frac{1}{30}\nabla p_{-4}^{(0)}\right)\\ \quad + \boldsymbol{r}\left(2p_{-2}^{(0)} + \frac{1}{2}p_{-3}^{(0)} + \frac{4}{15}p_{-4}^{(0)}\right)\end{array}\right], \tag{3.11}$$

$$p_e^{(0)} = p_{-2}^{(0)} + p_{-3}^{(0)} + p_{-4}^{(0)}, \tag{3.12}$$

where complete expressions of the growing and decaying spherical solid harmonics are given in appendix A.

The drop velocity is determined from the force-free condition. The total force acting on the drop is given by (Im & Kang 2003; Bandopadhyay *et al.* 2016)

$$\begin{aligned}\boldsymbol{F} = \boldsymbol{F}^H + M\boldsymbol{F}^E &= \int_A (\boldsymbol{\tau}_e^H \cdot \boldsymbol{e}_r)\,\mathrm{d}A + M\int_A (\boldsymbol{\tau}_e^E \cdot \boldsymbol{e}_r)\,\mathrm{d}A \\ &= -4\pi\nabla(r^3 p_{-2}) + M\int_A (\boldsymbol{\tau}_e^E \cdot \boldsymbol{e}_r)\,\mathrm{d}A, \end{aligned} \tag{3.13}$$

where the integration is performed on the drop surface (i.e. $\mathrm{d}A = r_s^2 \sin\theta\,\mathrm{d}\theta\,\mathrm{d}\phi$). Now, using the perturbation expansion (2.4), at the leading order of approximation we obtain

$$\boldsymbol{F}^{(0)} = \boldsymbol{F}^{H(0)} + M\boldsymbol{F}^{E(0)} = -4\pi\nabla(r^3 p_{-2}^{(0)}) + M\int_A (\boldsymbol{\tau}_e^{E(0)} \cdot \boldsymbol{e}_r)\,\mathrm{d}A. \tag{3.14}$$

At the leading order of approximation, the net electrical force on the drop ($\boldsymbol{F}^{E(0)}$) is identically zero, as the drop is electrically neutral and the applied electric field is uniform at far field. Therefore, the force-free condition at leading order is given by

$$\nabla(r^3 p_{-2}^{(0)}) = \boldsymbol{0}, \tag{3.15}$$

where $p_{-2}^{(0)} = r^{-2}[A_{-2,0}^{(0)} P_{1,0} + (A_{-2,1}^{(0)} \cos\phi + \hat{A}_{-2,1}^{(0)} \sin\phi) P_{1,1}]$. After substitution of the expressions for $A_{-2,0}^{(0)}$, $A_{-2,1}^{(0)}$ and $\hat{A}_{-2,1}^{(0)}$, the drop velocity at the leading order, $\boldsymbol{U}_d^{(0)} = U_{dx}^{(0)}\boldsymbol{e}_x + U_{dy}^{(0)}\boldsymbol{e}_y + U_{dz}^{(0)}\boldsymbol{e}_z$, is obtained as

$$\left.\begin{aligned} U_{dx}^{(0)} = U_{dy}^{(0)} &= 0, \\ U_{dz}^{(0)} &= k_0 + \left(\frac{\lambda}{3\lambda+2}\right) k_2. \end{aligned}\right\} \tag{3.16}$$

To determine the deformed drop shape, we express $f^{(Ca)}$ in terms of linear combinations of surface harmonics of the form (Hetsroni & Haber 1970)

$$f^{(Ca)} = \sum_{n=1}^{\infty}\sum_{m=0}^{n} [L_{n,m}^{(Ca)} \cos(m\phi) + \hat{L}_{n,m}^{(Ca)} \sin(m\phi)] P_{n,m}. \tag{3.17}$$

The unknown coefficients $L_{n,m}^{(Ca)}$ and $\hat{L}_{n,m}^{(Ca)}$ are obtained by using the normal stress balance boundary condition (the last boundary condition of (2.10)) in the following form

$$\left.\begin{aligned} L_{2,0}^{(Ca)} = -\frac{3}{8}\left(\frac{M(E_x^2 - 2E_z^2)}{(R+2)^2}\right)\Omega_T, \quad L_{2,1}^{(Ca)} &= \frac{3}{4}\left(\frac{ME_zE_x}{(R+2)^2}\right)\Omega_T + \frac{1}{24}\left(\frac{19\lambda+16}{\lambda+1}\right)k_1, \\ L_{2,2}^{(Ca)} = \frac{3}{16}\left(\frac{ME_x^2}{(R+2)^2}\right)\Omega_T, \quad L_{3,0}^{(Ca)} &= -\frac{1}{40}\left(\frac{11\lambda+10}{\lambda+1}\right)k_2, \\ L_{3,2}^{(Ca)} &= \frac{1}{240}\left(\frac{11\lambda+10}{\lambda+1}\right)k_2, \end{aligned}\right\} \tag{3.18}$$

where $\Omega_T = R^2 + 1 - 2S + (3/5)(((R-S)(3\lambda+2))/(\lambda+1))$ is the Taylor discriminating function (Saville 1997). Ω_T signifies the fact that the drop will be stretched parallel to the applied electric field (i.e. prolate shape) if $\Omega_T > 0$ and the reverse happens (the drop will be stretched normal to the applied electric field (i.e. oblate shape)) for $\Omega_T < 0$ when the drop is acted upon by a uniform electric field in an otherwise quiescent medium.

3.3. $O(Re_E)$ solution: effect of surface charge convection

After obtaining the electric and flow fields at the leading order, we now obtain the solution to (2.11) and (2.13) using the boundary conditions (2.12) and (2.14), respectively. At $O(Re_E)$, the electric field is induced due to charge convection, as there is no applied electric field at this order. The effect of charge convection is apparent from the given boundary condition (Bandopadhyay *et al.* 2016): $\boldsymbol{e}_r \cdot (R\boldsymbol{\nabla}\psi_i^{(Re_E)} - \boldsymbol{\nabla}\psi_e^{(Re_E)}) = -\boldsymbol{\nabla}_s \cdot (q_s^{(0)}\boldsymbol{V}_s^{(0)})$ applied at $r = 1$. The leading-order charge distribution and surface velocity are responsible for the alteration in the $O(Re_E)$ charge conservation equation at the drop surface. To obtain the non-zero surface harmonics present in the $O(Re_E)$ electric potential, we first evaluate the term $\boldsymbol{\nabla}_s \cdot (q_s^{(0)}\boldsymbol{V}_s^{(0)})$ at $r = 1$ in the following form (Kim & Karrila 1991)

$$\boldsymbol{\nabla}_s \cdot (q_s^{(0)}\boldsymbol{V}_s^{(0)}) = 2(q_s^{(0)}\boldsymbol{V}_s^{(0)} \cdot \boldsymbol{e}_r) + \frac{1}{\sin\theta}\frac{\partial}{\partial\theta}(q_s^{(0)}\boldsymbol{V}_s^{(0)} \cdot \boldsymbol{e}_\theta) + \frac{1}{\sin\theta}\frac{\partial}{\partial\phi}(q_s^{(0)}\boldsymbol{V}_s^{(0)} \cdot \boldsymbol{e}_\phi). \quad (3.19)$$

Now, we substitute the expressions of the surface velocity field ($\boldsymbol{V}_s^{(0)}$) and the surface charge distribution ($q_s^{(0)}$) in (3.19). We represent the right-hand side of (3.19) in terms of various surface harmonics by using the orthogonality of the spherical surface harmonics as

$$\begin{aligned} &-2(q_s^{(0)}\boldsymbol{V}_s^{(0)} \cdot \boldsymbol{e}_r) - \frac{1}{\sin\theta}\frac{\partial}{\partial\theta}(q_s^{(0)}\boldsymbol{V}_s^{(0)} \cdot \boldsymbol{e}_\theta) - \frac{1}{\sin\theta}\frac{\partial}{\partial\phi}(q_s^{(0)}\boldsymbol{V}_s^{(0)} \cdot \boldsymbol{e}_\phi) \\ &= \sum_{n=0}^{\infty}\sum_{m=0}^{n}[Z_{n,m}\cos(m\phi) + \hat{Z}_{n,m}\sin(m\phi)]P_{n,m}. \end{aligned} \quad (3.20)$$

The non-zero $Z_{n,m}$ and $\hat{Z}_{n,m}$ terms are obtained by invoking the orthogonality of associated Legendre polynomial and complete expressions are given in appendix B. These non-zero surface harmonics suggest that the electric potential at $O(Re_E)$ should be of the form

$$\left.\begin{aligned} \psi_i^{(Re_E)} &= \sum_{n=1}^{4} r^n \sum_{m=0}^{n} a_{n,m}^{(Re_E)}\cos(m\phi)P_{n,m}, \\ \psi_e^{(Re_E)} &= \sum_{n=1}^{4} r^{-n-1} \sum_{m=0}^{n} b_{-n-1,m}^{(Re_E)}\cos(m\phi)P_{n,m}. \end{aligned}\right\} \quad (3.21)$$

Now, invoking this form of the electric potential in the boundary conditions (2.12) we obtain the unknown coefficients present in the $O(Re_E)$ electric potential which are given in appendix C. The charge distribution at the drop interface at $O(Re_E)$ is obtained as

$$q_s^{(Re_E)} = \left(S\frac{\partial\psi_i^{(Re_E)}}{\partial r} - \frac{\partial\psi_e^{(Re_E)}}{\partial r}\right)\Bigg|_{r=1} = \sum_{n=1}^{4}\sum_{m=0}^{n}\left\{\frac{n(1+S)+1}{n(1+R)+1}\right\}Z_{n,m}\cos(m\phi)P_{n,m}. \quad (3.22)$$

At $O(Re_E)$, the velocity and pressure fields are generated solely by the Maxwell stresses present at the drop surface due to the $O(Re_E)$ electric field (Bandopadhyay *et al.* 2016). The $O(Re_E)$ velocity and pressure fields can be expressed in terms of spherical solid harmonics as outlined in (3.2)–(3.5). Non-zero spherical solid

harmonics exist up to $n = 5$ and can be obtained by using the boundary conditions given in (2.14). Complete expressions for the $O(Re_E)$ flow field are too lengthy to be presented here. However, we have included the method for obtaining the $O(Re_E)$ solid harmonics and also the general expression for these in the supplementary material available at https://doi.org/10.1017/jfm.2016.677.

The drop velocity can be obtained by using the force-free condition at $O(Re_E)$ as

$$\boldsymbol{F}^{(Re_E)} = -4\pi\nabla(r^3 p_{-2}^{(Re_E)}) = \boldsymbol{0}, \tag{3.23}$$

where $p_{-2}^{(Re_E)} = r^{-2}[A_{-2,0}^{(Re_E)} P_{1,0} + (A_{-2,1}^{(Re_E)} \cos\phi + \hat{A}_{-2,1}^{(Re_E)} \sin\phi) P_{1,1}]$. The coefficients $A_{-2,0}^{(Re_E)}$, $A_{-2,1}^{(Re_E)}$ and $\hat{A}_{-2,1}^{(Re_E)}$ are mentioned in appendix D. The $O(Re_E)$ drop velocity is obtained as

$$\left.\begin{aligned} U_{dx}^{(Re_E)} &= \frac{6}{35}\frac{ME_xE_z(R-S)(3R-S+3)(2\lambda^2+63\lambda+45)k_2}{(3\lambda+2)^2(\lambda+1)(\lambda+4)(R+2)^2(3+2R)}, \\ U_{dz}^{(Re_E)} &= \frac{6}{35}\frac{M(R-S)(3R-S+3)\{(36\lambda^2+119\lambda+75)E_x^2+(8\lambda^2+42\lambda+40)E_z^2\}k_2}{(3\lambda+2)^2(\lambda+1)(\lambda+4)(R+2)^2(3+2R)}. \end{aligned}\right\} \tag{3.24}$$

3.4. $O(Ca)$ solution: effect of shape deformation

At $O(Ca)$, the electric field is induced due to shape deformation of the drop, as there is no applied electric field at this order. We obtain the $O(Ca)$ electric potential inside and outside the drop as

$$\left.\begin{aligned} \psi_i^{(Ca)} &= \sum_{n=1}^{2} r^n \sum_{m=0}^{n} a_{n,m}^{(Ca)} \cos(m\phi) P_{n,m}, \\ \psi_e^{(Ca)} &= \sum_{n=1}^{4} r^{-n-1} \sum_{m=0}^{n} b_{-n-1,m}^{(Ca)} \cos(m\phi) P_{n,m}, \end{aligned}\right\} \tag{3.25}$$

where complete expressions of the unknown coefficients are given in appendix E. The charge distribution at the drop interface at $O(Ca)$ can be obtained as

$$q_s^{(Ca)} = \left[\begin{aligned} &S\left\{\frac{\partial\psi_i^{(Ca)}}{\partial r} + f\frac{\partial^2\psi_i^{(0)}}{\partial r^2} - \frac{\partial f}{\partial\theta}\frac{\partial\psi_i^{(0)}}{\partial\theta} - \frac{1}{\sin^2\theta}\frac{\partial f}{\partial\phi}\frac{\partial\psi_i^{(0)}}{\partial\phi}\right\}\Bigg|_{r=1} \\ &-\left\{\frac{\partial\psi_e^{(Ca)}}{\partial r} + f\frac{\partial^2\psi_e^{(0)}}{\partial r^2} - \frac{\partial f}{\partial\theta}\frac{\partial\psi_e^{(0)}}{\partial\theta} - \frac{1}{\sin^2\theta}\frac{\partial f}{\partial\phi}\frac{\partial\psi_e^{(0)}}{\partial\phi}\right\}\Bigg|_{r=1} \end{aligned}\right], \tag{3.26}$$

where the complete expression can be easily obtained by substituting the expressions for $\psi_{i,e}^{(0)}$ and $\psi_{i,e}^{(Ca)}$. At $O(Ca)$, the velocity and pressure fields are generated due to shape deformation and also due to the Maxwell stresses present at the drop surface due to the $O(Ca)$ electric field (Bandopadhyay *et al.* 2016). The $O(Ca)$ velocity and pressure fields can be expressed in terms of spherical solid harmonics as outlined in (3.2)–(3.5). Non-zero spherical solid harmonics exist up to $n = 6$ and can be obtained by using the boundary conditions given in (2.19). Here also we do not provide complete expressions for the solid harmonics at $O(Ca)$ due to the excessive length of the algebraic expressions. However, we have provided the method to obtain these solid harmonics and also the general expression in the supplementary material.

The drop velocity can be obtained by using the force-free condition at $O(Ca)$ as

$$\boldsymbol{F}^{(Ca)} = -4\pi\boldsymbol{\nabla}(r^3 p_{-2}^{(Ca)}) = \boldsymbol{0}, \tag{3.27}$$

which yields the drop velocity as

$$\left.\begin{aligned} U_{dz}^{(Ca)} &= \frac{k_2\{L_{2,0}^{(Ca)} f_1 + L_{2,2}^{(Ca)} f_2\} + M\{L_{3,0}^{(Ca)}(E_x^2 f_3 + E_z^2 f_4) + L_{3,2}^{(Ca)} E_x^2 f_5\}}{35(3\lambda+2)(3\lambda^2+5\lambda+2)(\lambda+4)(2R^3+11R^2+20R+12)}, \\ U_{dx}^{(Ca)} &= \frac{k_2 L_{2,1}^{(Ca)} f_6 + L_{3,0}^{(Ca)}\{ME_x E_z f_7 + k_1 f_8\} + L_{3,2}^{(Ca)}\{ME_x E_z f_9 + k_1 f_{10}\}}{35(3\lambda+2)(3\lambda^2+5\lambda+2)(\lambda+4)(2R^3+11R^2+20R+12)}, \end{aligned}\right\} \tag{3.28}$$

where $f_1 - f_{10}$ are functions of R, S and λ. The complete expressions for $f_1 - f_{10}$ are given in appendix F.

3.5. *Drop trajectory*

Finally we obtain the combined effect of charge convection and shape deformation on the velocity of the drop by combining these two effects linearly as

$$\boldsymbol{U}_d = (U_{dz}^{(0)} + Re_E U_{dz}^{(Re_E)} + CaU_{dz}^{(Ca)})\boldsymbol{e}_z + (Re_E U_{dx}^{(Re_E)} + CaU_{dx}^{(Ca)})\boldsymbol{e}_x. \tag{3.29}$$

It is clear from the above equation that the drop has velocity components in both the axial direction (z-direction) as well as the transverse or cross-stream direction (x-direction) in the presence of a background plane Poiseuille flow and a uniform electric field. During the transverse motion, the drop encounters a spatially varying background flow which leads to a continuous variation of the flow field and electric potential inside and outside the drop (and subsequently the electric charge distribution at the drop surface). Due to this continuous adjustment of velocity and surface charges with the background flow, a drop which is migrating in the cross-stream direction will not be in a steady motion until it reaches the centreline of the flow. Towards making an analytical treatment, we have made a quasi-steady-state approximation in which the time required for the velocity and surface charge distributions to establish is much smaller than the time scale of drop motion. Now, we look into the criteria under which velocity and surface charges are established very quickly as compared with the time scale of drop motion. The velocity field is established in a time scale $t_v = \rho_e a^2/\mu_e$ (which is the viscous time scale), while the surface charge distribution is established in a time scale $t_e = \varepsilon_e/\sigma_e$ (which is the charge-relaxation time scale). On the other hand, the time scale of drop motion is $t_{d,x} = a/V_c U_{dx}$ (with $U_{dx} \sim Re_E M$ or $U_{dx} \sim Ca\,M$) for transverse motion and $t_{d,z} = a/V_c U_{dz}$ (with $U_{dz} \sim 1$) for axial motion. The criterion for the velocity field to establish instantaneously with respect to the spatially varying flow field can be obtained in the following form: (i) $t_v \ll t_{d,x} \Rightarrow Re\,Re_E M \ll 1$ (or $Re\,Ca\,M \ll 1$) and (ii) $t_v \ll t_{d,z} \Rightarrow Re \ll 1$. Among $Re\,Re_E M \ll 1$ (or $Re\,Ca\,M \ll 1$) and $Re \ll 1$, the second one is the more stringent criterion owing to the fact that the transverse motion of the drop is responsible for the time-varying characteristics that are expected. As we have assumed the flow field is governed by the Stokes equation (which is due to $Re \ll 1$), the criterion of the quasi-steady-state approximation for velocity field is satisfied. Following a similar method, the criterion for the surface charge distribution to adjust instantaneously with the spatially varying flow field can be obtained in the following form: (i) $t_e \ll t_{d,x} \Rightarrow Re_E^2 M \ll 1$ (or $Re_E Ca\,M \ll 1$) and (ii) $t_e \ll t_{d,z} \Rightarrow Re_E \ll 1$. Among $Re_E^2 M \ll 1$ (or $Re_E Ca\,M \ll 1$) and $Re_E \ll 1$, the second

one is the more stringent criterion. In the present analysis we have considered $Re_E \ll 1$, which satisfies the quasi-steady-state criterion. We have the analysis in the regime of low Re_E (or equivalently the regime of quasi-steady-state). Both the conditions above indicate that, under the assumptions of the present work, the velocity field and charge distribution occur at a time scale which is much faster than the characteristic system time scale. This renders the quasi-steady-state assumption valid. A similar quasi-steady-state approximation is also followed by Pak *et al.* (2014) in their study of motion of a surfactant-laden drop in Poiseuille flow. So, under this quasi-steady-state approximation, here we determine the quasi-steady-state drop trajectory. Towards this, we first substitute $k_0 = 4(x_d/H)(1 - x_d/H)$, $k_1 = (4/H)(1 - 2x_d/H)$ and $k_2 = -4/H^2$. Here x_d is the non-dimensional transverse position of the drop centroid (measured from the bottom wall), which may change with time, and H is the channel height. So, this representation of the plane Poiseuille flow considers $x_d = H/2$ as the channel centreline. To obtain the quasi-steady-state drop trajectory, we solve the following differential equations

$$\left.\begin{aligned} \frac{\mathrm{d}x_d(t)}{\mathrm{d}t} &= Re_E U_{dx}^{(Re_E)} + Ca\, U_{dx}^{(Ca)}, \\ \frac{\mathrm{d}z_d(t)}{\mathrm{d}t} &= U_{dz}^{(0)} + Re_E U_{dz}^{(Re_E)} + Ca\, U_{dz}^{(Ca)}, \end{aligned}\right\} \tag{3.30}$$

where z_d is the axial position of the drop centroid. $U_{dz}^{(0)}$, $U_{dx}^{(Ca)}$ and $U_{dz}^{(Ca)}$ are functions of x_d that can be easily obtained by substituting k_0, k_1 and k_2 in the expressions for the drop velocity. The cross-stream motion of the drop is of prime importance to us. Towards this we integrate equation (3.30) and obtain

$$x_d(t) = x_{d,\infty} + [x_{d,0} - x_{d,\infty}] \exp\left(-\frac{t}{t_m}\right), \tag{3.31}$$

where $x_{d,\infty}$ is the steady state transverse position of the drop (obtained as $t \to \infty$) and $x_{d,0}$ is the initial transverse position of the drop. An important quantity to note here is t_m, which is the characteristic cross-stream migration time scale that quantifies the time required by the drop to reach steady state velocity. The expressions for $x_{d,\infty}$ and t_m are obtained as

$$x_{d,\infty} = \left[\frac{H}{2} + ME_xE_z\left(f_{12} + \frac{Re_E}{Ca}f_{11}\right)H^2\right], \tag{3.32}$$

$$t_m = \frac{H^4}{Ca}f_{13}, \tag{3.33}$$

where f_{11} and f_{12} are known functions of R, S and λ, while f_{13} is a sole function of λ. The complete expressions for f_{11}, f_{12}, f_{13} are given in appendix G. It is important to note that (3.31), which represents the temporal evolution of transverse position of the drop, is only valid for $Ca > 0$. For the special case of $Ca = 0$, the temporal evolution of the transverse position of the drop is obtained as

$$x_d(t) = x_{d,0} + Re_E U_{dx}^{(Re_E)} t. \tag{3.34}$$

So, with increasing time, the transverse position of the drop (x_d) increases linearly. There is no steady state transverse position (as $t \to \infty$ gives $x_d \to \infty$). In a

practical situation the transverse position of the drop will increase, and after some finite time it will encounter the bounding wall. The presence of a bounding wall induces a hydrodynamic lift force on the drop perpendicular to the flow direction (Uijttewaal, Nijhof & Heethaar 1993; Uijttewaal & Nijhof 1995; Stan *et al.* 2011). This hydrodynamic lift force retards the drop motion towards the wall. So, the drop will eventually settle to some finite $x_{d,\infty}$ (i.e. $0 < x_{d,\infty} < H$) instead of the ever-increasing transverse position. As the present study assumes background flow to be unbounded (which means the drop is far away from the bounding walls), the present study is not able to predict $x_{d,\infty}$ in the limit of $Ca = 0$. So, at this point, one very important thing to note regarding the validity of (3.31) and (3.34) is that these equations are applicable to find the temporal evolution of the transverse position of the drop only when the drop is far away from the bounding walls.

4. Results and discussion

4.1. *Validation*

Before investigating the combined effect of uniform electric field and plane Poiseuille flow on the motion of the drop, we validate our analytical results with previously reported analytical results for two limiting cases. First, we consider the case of motion and deformation of a neutrally buoyant leaky dielectric drop in the presence of a uniform electric field in an otherwise quiescent medium (no imposed background flow). In this situation the drop remains stationary, but the drop deforms to an oblate/prolate shape in the following form

$$r_s = 1 + Ca\,M\left\{\frac{3}{4}\frac{1}{(R+2)^2}\left[R^2+1-2S+\frac{3}{5}\frac{(R-S)(3\lambda+2)}{(\lambda+1)}\right]P_{2,0}\right\}, \tag{4.1}$$

where we have substituted $\boldsymbol{E}_\infty = \boldsymbol{e}_z$ and $k_0 = k_1 = k_2 = 0$ in (3.18). This result has been previously obtained by Taylor (1966) and subsequently validated experimentally and numerically by others (Ha & Yang 2000*a*; Feng & Scott 2006; Vizika & Saville 2006; Lac & Homsy 2007). Second, we consider the case of the motion and deformation of a drop in plane Poiseuille flow (no externally applied electric field). In this case the drop moves in the flow direction, and if the drop is placed at an off-centreline location then the drop also experiences a cross-stream migration, as previously obtained by Chan & Leal (1979) and also obtained as a limiting case from our analytical results in the following form

$$\begin{aligned}\boldsymbol{U}_d = &\left[k_0+\left(\frac{\lambda}{3\lambda+2}\right)k_1\right]\boldsymbol{e}_z \\ &+Ca\left[\left(-\frac{k_1k_2}{210}\right)\frac{(198\lambda^5-1242\lambda^4-7327\lambda^3-6292\lambda^2+1843\lambda+2320)}{(3\lambda+2)^2(4+\lambda)(\lambda+1)^2}\right]\boldsymbol{e}_x\end{aligned} \tag{4.2}$$

by substituting $E_x = E_y = 0$ (or equivalently $M = 0$) in (3.29). The presence of background plane Poiseuille flow leads to deformation of the drop, which is obtained as

$$r_s = 1 + Ca\left[\begin{array}{l}\left\{\frac{1}{24}\left(\frac{19\lambda+16}{\lambda+1}\right)k_1\right\}\cos\phi P_{2,1} - \left\{\frac{1}{40}\left(\frac{11\lambda+10}{\lambda+1}\right)k_2\right\}P_{3,0} \\ \quad +\left\{\frac{1}{240}\left(\frac{11\lambda+10}{\lambda+1}\right)k_2\right\}\cos(2\phi)P_{3,2}\end{array}\right], \tag{4.3}$$

which has been previously obtained by Chan & Leal (1979).

4.2. *Combined effect of plane Poiseuille flow and uniform electric field on the drop motion*

The combined effect is not a mere linear combination of two distinct effects (plane Poiseuille flow and uniform electric field) because the electric potential and flow field are nonlinearly coupled by the charge convection and shape deformation in the following two ways: (i) the presence of background plane Poiseuille flow alters the charge distribution at the drop surface, which alters the electric potential, electric stresses, and subsequently modifies the flow field and hydrodynamic force, (ii) coupling through the shape deformation due to plane Poiseuille flow and uniform electric field. Shape deformation alters the electric potential, electrical stresses, flow field, and ultimately the hydrodynamic force on the drop. The mathematical expressions for the combined effect of plane Poiseuille flow and uniform electric field on the drop velocity in the axial as well as transverse directions can be obtained by substituting different terms in (3.29). In an effort to disentangle the effects of the plane Poiseuille flow and the electric field on the axial and transverse (or cross-stream) velocities of the drop, we rearrange the drop velocity as

$$\begin{aligned} U_{dz} &= U_{dz}^{(0)} + Re_E U_{dz}^{(Re_E)} + Ca\, U_{dz}^{(Ca)} \\ &= \underbrace{k_0 + \left(\frac{\lambda}{3\lambda+2}\right) k_1}_{\Delta_1} + \underbrace{Re_E k_2 M \Gamma_2}_{\Delta_2} + \underbrace{Ca\, k_2 M \Gamma_1}_{\Delta_3}, \end{aligned} \tag{4.4}$$

$$\begin{aligned} U_{dx} &= Re_E U_{dx}^{(Re_E)} + Ca\, U_{dx}^{(Ca)} \\ &= \underbrace{Re_E k_2 M E_x E_z \Gamma_3}_{\Delta_4} + \underbrace{Ca\, k_1 k_2 \Gamma_4}_{\Delta_5} + \underbrace{Ca\, k_2 M E_x E_z \Gamma_5}_{\Delta_6}, \end{aligned} \tag{4.5}$$

where Γ_1 and Γ_2 are known functions of R, S, λ, E_x and E_z, while Γ_3, Γ_4 and Γ_5 are known functions of R, S and λ. Expressions for Γ_1–Γ_5 can be easily obtained by comparing (4.4) and (4.5) with (3.24) and (3.28), respectively. The term Δ_1 represents the axial velocity of the drop in plane Poiseuille flow in the absence of shape deformation and charge convection. The terms Δ_2 and Δ_3 represent the alteration in drop velocity in the axial direction due to charge convection and shape deformation, respectively. A closer look into the expressions for Δ_2 and Δ_3 reveals that these two terms are non-zero if $k_2 M \neq 0$. Hence, an externally applied uniform electric field affects the axial velocity of the drop only in the presence of flow curvature (i.e. $k_2 \neq 0$). The term Δ_4 present in (4.5) signifies the effect of charge convection on the cross-stream migration velocity, while Δ_5 and Δ_6 represent the effect of shape deformation on the cross-stream migration velocity. Δ_5 arises owing to the shape deformation, which is solely due to the plane Poiseuille flow. A closer look into the expression for Δ_4 and Δ_6 reveals that these terms are non-zero if $k_2 M E_x E_z \neq 0$. Hence, the electric field affects the cross-stream migration of the drop in the presence of flow curvature (i.e. $k_2 \neq 0$) if and only if the electric field is tilted (i.e. $E_x E_z \neq 0$). This means if the applied electric field ($\boldsymbol{E}_\infty$) is acting along the axial direction ($\boldsymbol{E}_\infty = \boldsymbol{e}_z$) or acting along the transverse direction ($\boldsymbol{E}_\infty = \boldsymbol{e}_x$), there is no effect of electric field on the cross-stream migration velocity of the drop. So, the necessary condition for the applied electric field to make any change on the cross-stream migration velocity of the drop is that it has to be a tilted electric field with respect to the imposed flow direction. The tilt angle, defined as $\theta_t = \tan^{-1}(E_x/E_z)$, should satisfy the following criterion: $0 < \theta_t < \pi/2$ or $\pi/2 < \theta_t < \pi$ to affect the cross-stream migration of the drop. It must be noted that the presence of an electric field always affects the axial velocity of the drop (U_{dz}), irrespective of its direction of application.

4.2.1. *Drop velocity*

It is evident from (4.4) and (4.5) that there are two important effects which alter the drop velocity: charge convection (the strength of which is represented by Re_E) and shape deformation (the strength of which is represented by Ca). In addition to these two dimensionless numbers, there are the following important electrohydrodynamic parameters which affect the drop motion: the relative strength of the components of applied electric field (E_x, E_z), the Mason number (M), the viscosity ratio (λ) and the electrical property ratios (R, S). The effect of these parameters on the cross-stream migration velocity (U_{dx}) and steady state transverse position of the drop ($x_{d,\infty}$) are of prime importance. Before presenting the effect of charge convection and shape deformation on the drop velocity and drop trajectory, we investigate the physical reasons behind the charge-convection-induced and shape-deformation-induced cross-stream migration of a drop.

In the present study, in the presence of a tilted electric field and background plane Poiseuille flow, we have obtained not only alteration in the axial drop velocity but also a non-intuitive cross-stream migration of the drop due to charge-convection effects, which is denoted by $U_{dx}^{(Re_E)}$. The effect of charge convection on the cross-stream migration velocity can be well understood if we systematically investigate the charge distribution at the drop surface and alteration of the same due to fluid flow. Towards this we consider three representative cases: Case I with axial electric field $\boldsymbol{E}_\infty = \boldsymbol{e}_z$ (or $\theta_t = 0$), Case II with transverse electric field $\boldsymbol{E}_\infty = \boldsymbol{e}_x$ (or $\theta_t = \pi/2$) and Case III with tilted electric field $\boldsymbol{E}_\infty = (\boldsymbol{e}_x + \boldsymbol{e}_z)/\sqrt{2}$ (or $\theta_t = \pi/4$). Next we show the effect of fluid flow on the surface charge distribution. We show the contour plot of the surface charge density, q_s. To represent the explicit variation of surface charge density with θ and ϕ, we also plot the variation of $q_s(\theta)$ for $\phi = \pi/4,\ 3\pi/4$ and the variation of $q_s(\phi)$ for $\theta = \pi/4,\ 3\pi/4$. The choice of two ϕ values while showing the variation of $q_s(\theta)$ is made so that two ϕ values are symmetrically located with respect to the axial plane ($\phi = \pi/2$). Likewise, the choice of two θ values while showing the variation of $q_s(\phi)$ is made so that two θ values are symmetrically located with respect to the transverse plane ($\theta = \pi/2$).

Case I (axial electric field). In figure 2(*a–c*) we show the charge distribution on the drop surface in the presence of an axial electric field ($\boldsymbol{E}_\infty = \boldsymbol{e}_z$ or $\theta_t = 0$) while the background flow is considered as plane Poiseuille flow. The parameters used to calculate the charge distribution are given in the figure caption. In the absence of charge convection (i.e. $Re_E = 0$), the contour plot of the surface charge density, $q_s^{(0)}$, is depicted in figure 2(*a*). Figure 2(*a*) shows that the surface charge distribution is symmetric about the axial plane and antisymmetric about the transverse plane. Explicit variation of the surface charge density with θ is depicted in figure 3(*a*), which shows that when $Re_E = 0$ the variation of $q_s(\theta)$ is antisymmetric about the $\theta = \pi/2$ plane. Figure 3(*a*) also depicts that the variation of $q_s(\theta)$ is independent of ϕ, which signifies the symmetry of surface charge density about the axial plane. The charge distribution coupled with a tangential electric field creates a tangential electric force (F_θ^E) which is the jump of tangential electric stress across the drop interface and can be obtained as $F_\theta^E = q_s(\boldsymbol{E} \cdot \boldsymbol{e}_\theta)$. The distribution of the tangential electric force (F_θ^E) with θ is represented in figure 3(*b*), which shows that F_θ^E is also antisymmetric about the transverse plane. Hence, the flow field generated due to this antisymmetric electric force (F_θ^E) in the presence of $\boldsymbol{E}_\infty = \boldsymbol{e}_z$ is also antisymmetric, which finally leads to zero electrohydrodynamic force on the drop. This is the physical picture in the absence of charge convection (i.e. $Re_E = 0$). An interesting thing happens

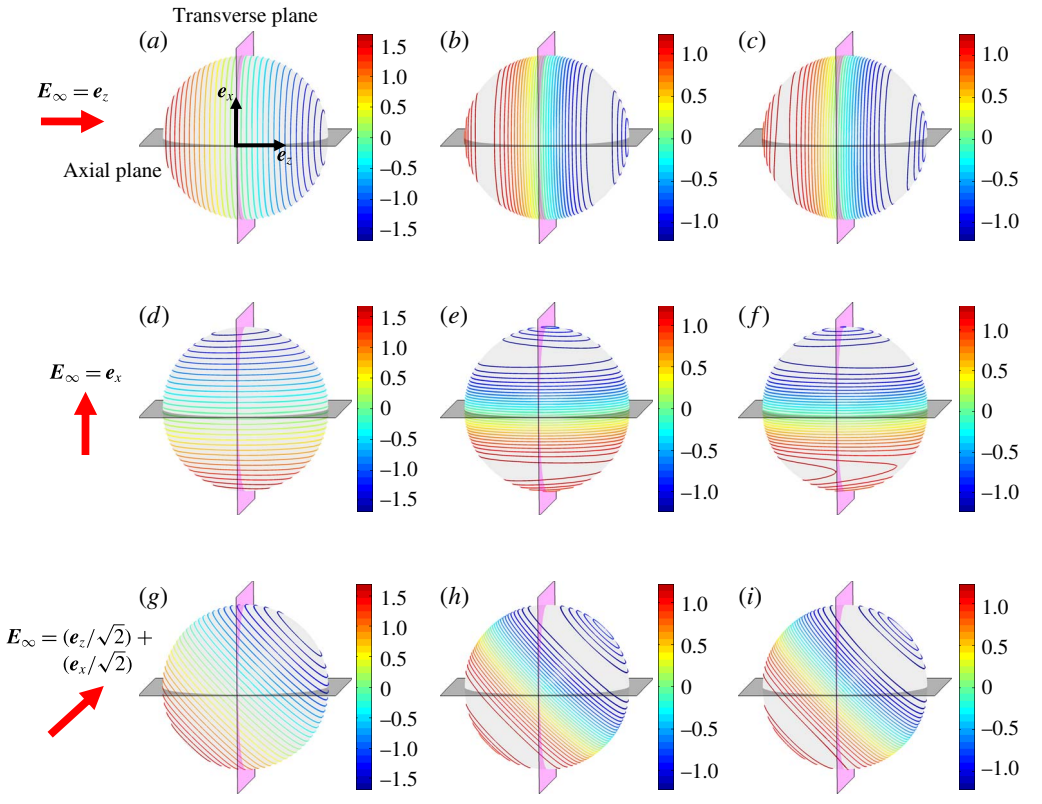

FIGURE 2. (Colour online) This representation depicts the charge distribution at the drop surface. Charge distribution in (*a–c*) axial (Case I), (*d–f*) transverse (Case II) and (*g–i*) tilted (Case III) electric fields, respectively. (*a*,*d*,*g*) $q_s^{(0)}$, (*b*,*e*,*h*) $q_s^{(0)} + Re_E q_s^{(Re_E)}$ at $x_d = 5$ (centreline), and (*c*,*f*,*i*) $q_s^{(0)} + Re_E q_s^{(Re_E)}$ at $x_d = 4$ (off-centreline), respectively. The parameters employed are $R = 0.5$, $S = 2$, $M = 2$, $\lambda = 0.2$, $Re_E = 0.2$ and $H = 10$. Colourbar represents the magnitude of the dimensionless surface charge density.

when we consider the charge-convection effect. The surface charge convection in the presence of plane Poiseuille flow markedly alters the charge distribution on the drop surface, as shown in figure 2(*b*,*c*). Figure 2(*b*) depicts the contours of the surface charge density, $q_s^{(0)} + Re_E q_s^{(Re_E)}$, when the drop is at the centreline ($x_d = 5$, considering $H = 10$) of the imposed flow. Comparison between $Re_E = 0$ and $Re_E = 0.2$ curves of figure 3(*a*) reveals that there is a significant reduction in charge density near $\theta = 0$ and π for $Re_E = 0.2$. This reduction in charge density is due to the velocity field at the drop interface. The tangential velocity field in the absence of charge convection is shown as an inset of figure 3(*a*). This leading-order tangential velocity at the drop surface is a linear combination of tangential velocities in a uniform electric field and plane Poiseuille flow. Combination of the uniform electric field and plane Poiseuille makes $V_{s,\theta}^{(0)}$ asymmetric about the transverse plane. The tangential velocity ($V_{s,\theta}^{(0)}$) is positive near $\theta = 0$ and negative near $\theta = \pi$. This velocity distribution drives the charges away from $\theta = 0$, π and creates an asymmetric charge distribution about the transverse plane. The asymmetry of charge distribution about the transverse plane is more clearly depicted in figure 3(*c*), in which we show the variation of charge distribution with ϕ for $\theta = \pi/4$ and $3\pi/4$. Here, we plot the magnitude of the charge

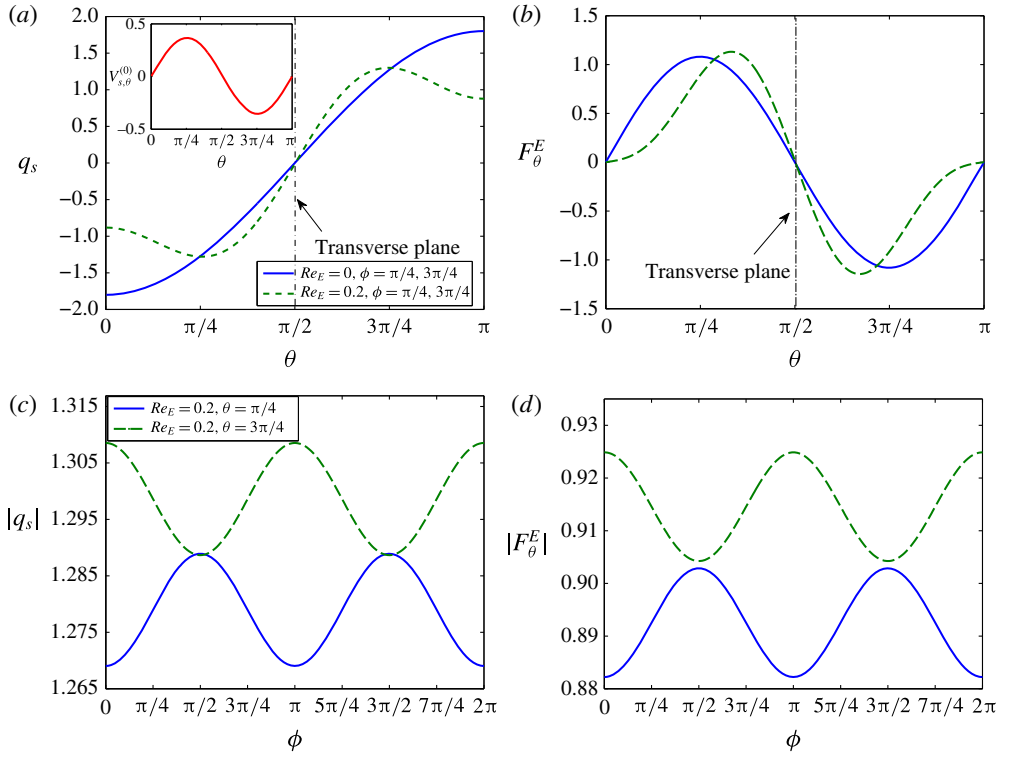

FIGURE 3. (Colour online) (*a*) Variation of $q_s(\theta)$ for $\phi = \pi/4,\ 3\pi/4$ considering $x_d = 5$. (*b*) Variation of $F^E_\theta(\theta)$ for $\phi = \pi/4,\ 3\pi/4$ considering $x_d = 5$. (*c*) Variation of $q_s(\phi)$ for $\theta = \pi/4,\ 3\pi/4$ considering $x_d = 5$. (*d*) Variation of $F^E_\theta(\phi)$ for $\theta = \pi/4,\ 3\pi/4$ considering $x_d = 5$. The parameters employed are $R = 0.5$, $S = 2$, $M = 2$, $\lambda = 0.2$ and $H = 10$.

density, $|q_s|$, so that the variation for both θ is noticeable. In the absence of charge convection (i.e. $Re_E = 0$), $q_s(\theta = \pi/4) = -q_s(\theta = 3\pi/4)$ for any ϕ, which signifies the antisymmetric charge distribution about the transverse plane. But when $Re_E = 0.2$, the magnitude of charge density at $\theta = \pi/4$ is very much different as compared with the magnitude of charge density at $\theta = 3\pi/4$. This asymmetric structure creates an asymmetric distribution of the tangential electric force, as depicted in figure 3(*d*). An asymmetric F^E_θ creates asymmetric electrohydrodynamic flow, which finally yields a net electrohydrodynamic force on the drop and an alteration in the drop velocity in the axial direction. There is no electrohydrodynamic force in the transverse direction. This is due to the fact that the charge distribution about the axial plane remains symmetric even in the presence of charge convection. This is reflected by the ϕ independence of $q_s(\theta)$ and $F^E_\theta(\theta)$ in figure 3(*a*) and figure 3(*b*), respectively.

When the drop is at an off-centreline location ($x_d = 4$), the contours of surface charge density are depicted in figure 2(*c*). To investigate the asymmetry in the charge distribution and associated electric force, we plot the variation of q_s and F^E_θ with θ and ϕ in figure 4(*a–d*). Figure 4(*a*) depicts that the variations of charge distribution with θ for $\phi = \pi/4$ and $\phi = 3\pi/4$ are different, which signifies asymmetry about the axial plane. Similar asymmetry is also found in the variation of the electric force in figure 4(*b*). Asymmetry about the axial plane arises for a drop with an off-centreline position because in this situation the drop encounters a different velocity at different

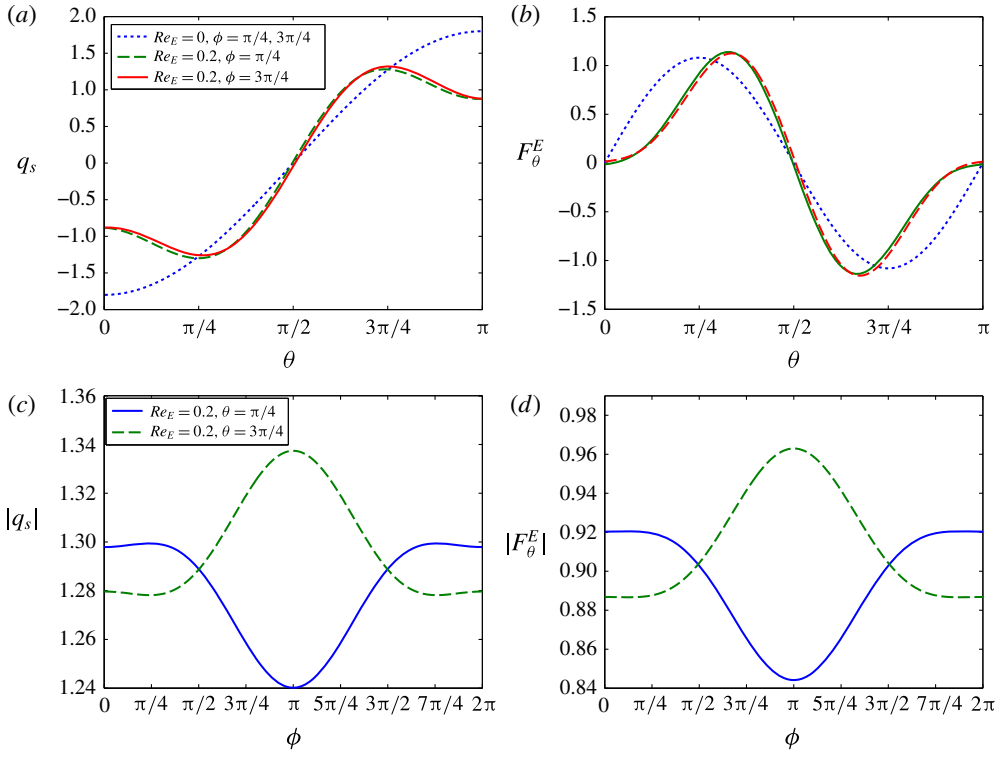

FIGURE 4. (Colour online) (*a*) Variation of $q_s(\theta)$ for $\phi = \pi/4,\ 3\pi/4$ considering $x_d = 4$. (*b*) Variation of $F^E_\theta(\theta)$ for $\phi = \pi/4,\ 3\pi/4$ considering $x_d = 4$. (*c*) Variation of $q_s(\phi)$ for $\theta = \pi/4,\ 3\pi/4$ considering $x_d = 4$. (*d*) Variation of $F^E_\theta(\phi)$ for $\theta = \pi/4,\ 3\pi/4$ considering $x_d = 4$. The parameters employed are $R = 0.5$, $S = 2$, $M = 2$, $\lambda = 0.2$ and $H = 10$.

ϕ positions. On the other hand, figure 4(*c*) depicts that the variations of charge distribution with ϕ for $\theta = \pi/4$ and $\theta = 3\pi/4$ are different, which signifies asymmetry about the transverse plane. Similar asymmetry is found in the variation of electric force in figure 4(*d*). The asymmetry in the charge distribution and electric force about the transverse plane finally creates an asymmetric electrohydrodynamic flow across the transverse plane, which yields a change in drop velocity in the axial direction. Notably, the asymmetry in the charge distribution and electric force about the axial plane also creates an asymmetric electrohydrodynamic flow around the drop interface. But this electrohydrodynamic flow is such that the net electrohydrodynamic force vanishes. However, asymmetry in the charge distribution and electric force creates a non-zero electrical torque of the form

$$\boldsymbol{T}^{E(Re_E)} = \int_A \boldsymbol{e}_r \times (\boldsymbol{\tau}_e^{E(Re_E)} \cdot \boldsymbol{e}_r)\, \mathrm{d}A = Re_E \left[\frac{24\pi}{5}\frac{(R-S)(2+5\lambda)}{(R+2)^2(\lambda+1)}\left(\frac{x_d}{H}\right)\left(1-\frac{2x_d}{H}\right)\right]\boldsymbol{e}_y. \tag{4.6}$$

An important thing to note here is that the direction of the electric torque is determined by the R/S ratio and x_d. This electric torque is exactly balanced by the torque due to the hydrodynamic stresses, which causes the drop to be torque-free

$$\boldsymbol{T}^{H(Re_E)} + M\boldsymbol{T}^{E(Re_E)} = \boldsymbol{0}, \tag{4.7}$$

where the hydrodynamic torque acting on the drop is obtained from (Happel & Brenner 1981) $\boldsymbol{T}^{H(Re_E)} = -8\pi\boldsymbol{\nabla}(r^3\chi_{-2}^{(Re_E)})$.

Case II (transverse electric field). In the presence of a transverse electric field ($\boldsymbol{E}_\infty = \boldsymbol{e}_x$ or $\theta_t = \pi/2$), the charge distribution on the drop surface is shown in figure 2(*d–f*). Contrary to Case I, here we do not obtain a change in the drop velocity in the direction of the applied external electric field. The effect of surface charge convection leads to an asymmetric charge distribution across the transverse plane, which leads to alteration in the drop velocity in the axial direction only. The charge distribution across the axial plane remains antisymmetric for $x_d = 5$ (refer to figure 2*e*). However, for the case of $x_d = 4$ (drop positioned at an off-centreline location), similar to Case I the asymmetry in the charge distribution about the axial plane (refer to figure 2*f*) leads to the generation of an electric torque in the y-direction as

$$\boldsymbol{T}^{E(Re_E)} = Re_E\left[\frac{24\pi}{5}\frac{(R-S)(8+5\lambda)}{(R+2)^2(\lambda+1)}\left(\frac{x_d}{H}\right)\left(1-\frac{2x_d}{H}\right)\right]\boldsymbol{e}_y, \tag{4.8}$$

which is further balanced by the hydrodynamic torque so as to satisfy the torque-free condition.

Case III (tilted electric field). The charge distribution due to the application of a tilted uniform electric field having both axial and transverse components is shown in figure 2(*g–i*) by considering $\boldsymbol{E}_\infty = (\boldsymbol{e}_x + \boldsymbol{e}_z)/\sqrt{2}$ or $\theta_t = \pi/4$. In this situation, the charge distribution becomes asymmetric about both the axial as well as the transverse planes even when the drop is at the centreline ($x_d = 5$) (refer to figure 2*h*). This leads to cross-stream migration of the drop in the x-direction along with alteration in the axial velocity as well. In this case also the drop experiences an electrical torque of the form

$$\boldsymbol{T}^{E(Re_E)} = Re_E\left[\frac{24\pi(R-S)}{(R+2)^2}\left(\frac{x_d}{H}\right)\left(1-\frac{2x_d}{H}\right)\right]\boldsymbol{e}_y, \tag{4.9}$$

which is further balanced by the hydrodynamic torque. So, the charge convection leads to an alteration in axial drop velocity when the charge distribution about the transverse place is asymmetric. The asymmetric charge distribution about the axial plane always leads to generation of electric torque on the drop. But the asymmetric charge distribution about the axial plane alters the cross-stream velocity of the drop only when the applied electric field has both axial and transverse components. This new mechanism of cross-stream migration of the drop in the presence of background plane Poiseuille flow is very different from dielectrophoresis (in which a uncharged particle moves in a non-uniform electric field) or electrophoresis (in which a charged particle moves in an electric field) because here the drop has zero net charge and the applied electric field is uniform.

An important thing to note from (4.5) is that the direction of the charge-convection-induced cross-stream migration velocity of the drop (which means sign of $U_{dx}^{(Re_E)}$) is determined by the components of the applied electric field (E_x, E_z), or equivalently the tilt angle (θ_t) and electrical property ratios (R, S), which is given by the term $G_{Re_E} = E_xE_z(S-R)(3R-S+3)$. When $G_{Re_E} > 0$, the drop migrates in the positive x-direction, and the reverse happens (drop migrates in the negative x-direction) for $G_{Re_E} < 0$. This migration velocity is independent of the transverse location of the drop. To show the effect of R and S on the charge-convection-induced cross-stream velocity of the drop, we construct a regime diagram showing the sign of $U_{dx}^{(Re_E)}$ (figure 5*a* for $\theta_t = \pi/4$

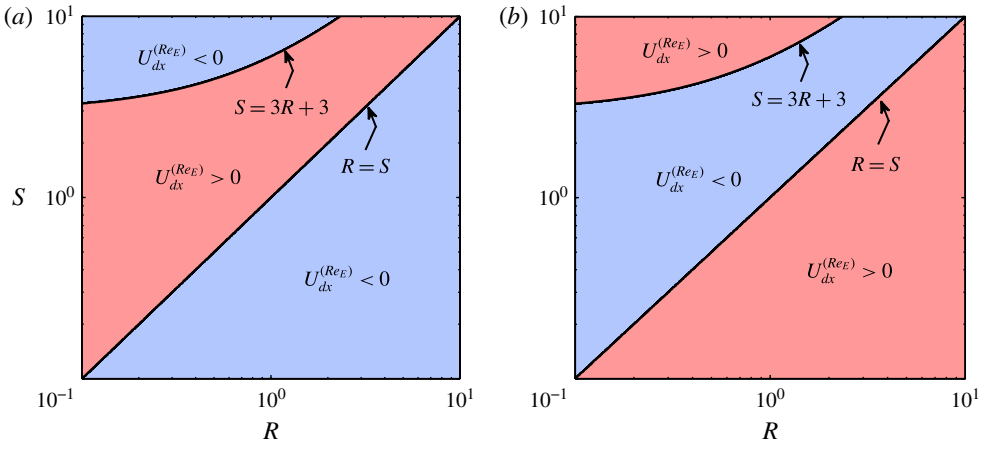

FIGURE 5. (Colour online) Sign of charge-convection-induced cross-stream migration velocity of the drop ($U_{dx}^{(Re_E)}$) on R–S plane for (*a*) $\theta_t = \pi/4$ and (*b*) $\theta_t = 3\pi/4$.

and figure 5*b* for $\theta_t = 3\pi/4$) in the R–S plane. From figure 5 it is clear that the two curves $R = S$ and $S = 3R + 3$ indicate the lines of zero charge-convection-induced cross-stream velocity ($U_{dx}^{(Re_E)} = 0$) even in the presence of a tilted electric field. So, the mere presence of a tilted electric field is not a sufficient condition for charge-convection-induced cross-stream motion of the drop in plane Poiseuille flow. However, $R = S$ or $S = 3R + 3$ do not necessarily imply that the shape-deformation-induced drop migration in the cross-stream direction will be zero.

The effect of shape deformation in terms of Ca has been previously shown in several studies (Chan & Leal 1979; Mortazavi & Tryggvason 2000; Griggs, Zinchenko & Davis 2007; Wang & Dimitrakopoulos 2011; Chaudhury, Mandal & Chakraborty 2016) for the case of plane Poiseuille flow, but without any consideration of an electric field. In plane Poiseuille flow, if the drop is placed at an off-centre position, the drop shape becomes asymmetric with respect to the channel centreline, which leads to cross-stream migration of a deformable drop (Chan & Leal 1979; Leal 1980). Chan & Leal (1979) have studied the cross-stream migration of a deformable drop in plane Poiseuille flow analytically and found the dependence of $U_{dx}^{(Ca)}$ on λ as: the drop migrates towards the centreline for $\lambda < 0.5$ or $\lambda > 10$, and the drop migrates away from the centreline for $0.5 < \lambda < 10$. Here, the presence of an electric field leads to an additional deformation of the drop into an oblate/prolate shape which modulates the drop motion in the axial as well as the cross-stream directions. This alteration of drop velocity in the presence of shape deformation is due to two different reasons: first, the extra deformation caused by the electric field alters the shape (or equivalently the cross-sectional area in the axial and transverse directions) of the drop. This altered cross-sectional area can increase/decrease the hydrodynamic drag force acting on the drop. Second, the extra deformation alters the surface charge distribution. The surface charge distribution coupled with a tangential electric field leads to generation of a tangential electric force which can further drive electrohydrodynamic flow around the drop interface. An asymmetric distribution of surface charge and associated tangential electric force induce an asymmetric electrohydrodynamic flow which further yields an electrohydrodynamic force on the drop. So, similar to the charge convection, shape deformation also induces asymmetry in charge distribution and electric force

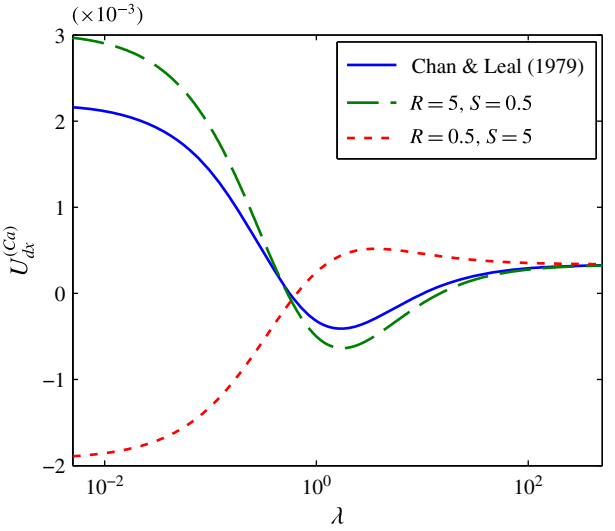

FIGURE 6. (Colour online) Variation of shape-deformation-induced cross-stream migration velocity of drop ($U_{dx}^{(Ca)}$) with viscosity ratio (λ). Other parameters have the following values $Ca = 0.1$, $M = 0.1$, $\theta_t = \pi/4$, $H = 10$ and $x_{d,0} = 4$.

depending on the direction of the electric field. Towards this, the most important thing to note here is that when the electric field is applied in the axial direction ($\boldsymbol{E}_\infty = \boldsymbol{e}_z$) or transverse direction ($\boldsymbol{E}_\infty = \boldsymbol{e}_x$), the shape-deformation-induced cross-stream migration due to the electric field is zero, which means the electric field does not affect $U_{dx}^{(Ca)}$. This is due to the fact that when $\boldsymbol{E}_\infty = \boldsymbol{e}_z$ or $\boldsymbol{E}_\infty = \boldsymbol{e}_x$ the drop becomes symmetrically stretched/compressed in the axial/transverse direction depending on the sign of the Taylor discriminating function Ω_T. The electric field contributes to the cross-stream migration in terms of shape deformation only when the electric field is tilted, because only then does the drop shape become asymmetric relative to the channel centreline. Figure 6 depicts that dependence of the shape-deformation-induced cross-stream migration velocity of the drop ($U_{dx}^{(Ca)}$) on λ is markedly altered due to the presence of the electric field. The electric field not only alters the magnitude of $U_{dx}^{(Ca)}$ but also the direction of drop migration, as is evident from figure 6 for the electrical property ratios $(R, S) = (0.5, 5)$.

Now, we show the combined effect of charge convection and shape deformation on the drop velocity. To explore the dependence of electrical property ratios, in figure 7 we plot the variation of $U_{dx}/U_{dx,\boldsymbol{E}_\infty=\boldsymbol{0}}$ in the R–S plane for the parameters specified in the figure caption. The colourbar represents the magnitude of $U_{dx}/U_{dx,\boldsymbol{E}_\infty=\boldsymbol{0}}$, where we have normalized U_{dx} by the cross-stream migration velocity of the drop in the absence of the electric field (represented by $U_{dx,\boldsymbol{E}_\infty=\boldsymbol{0}}$). Figure 7($a$) depicts that application of a uniform electric field dramatically alters the cross-stream velocity of the drop. Depending on the electrical property ratios (R, S), the cross-stream velocity of the drop can be much greater/less than the case of no electric field. An electric field not only changes the magnitude of the cross-stream migration velocity of the drop, but also can change the direction of migration, as depicted by figure 7(b) (represented by a negative value of $U_{dx}/U_{dx,\boldsymbol{E}_\infty=\boldsymbol{0}}$). However, the net effect due to the electric field will be decided by the magnitude of the governing parameters (Re_E, Ca, M, λ, R, S

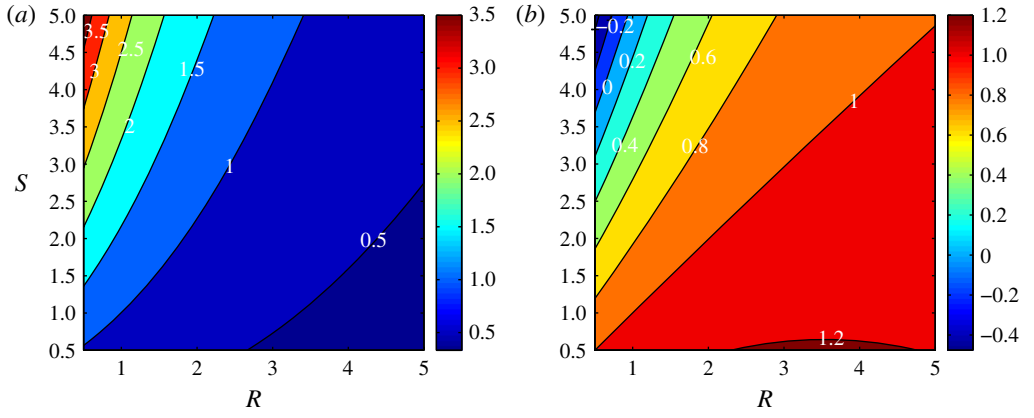

FIGURE 7. (Colour online) Combined effect of charge convection and shape deformation on the normalized cross-stream migration velocity of the drop ($U_{dx}/U_{dx,\boldsymbol{E}_\infty=\boldsymbol{0}}$) on the R–S plane for (*a*) $\lambda = 15$ and (*b*) $\lambda = 0.25$. Other parameters have the following values $Ca = 0.2$, $Re_E = 0.1$, $M = 0.1$, $\theta_t = \pi/8$, $H = 10$ and $x_{d,0} = 4$.

and θ_t). An interesting thing to note from figure 7 is that there are R, S values for which $U_{dx}/U_{dx,\boldsymbol{E}_\infty=\boldsymbol{0}} = 1$, which represents a zero net effect of the applied electric field on U_{dx}. Another interesting thing to note from figure 7(*b*) is that there is also a line of $U_{dx} = 0$ (line of zero cross-stream migration), which means the charge-convection and shape-deformation effects are individually zero at those property values or the combined effects of charge convection and shape deformation cancel each other.

An important limiting situation can be obtained by considering $R = S$, which represents a charge-free interface. This situation is similar to the case of a perfect dielectric drop suspended in another perfect dielectric medium. In this case the charge-convection-induced cross-stream migration velocity vanishes (this is also evident from the $R = S$ line shown in figure 5), but the shape-deformation-induced component of the cross-stream migration velocity remains non-zero, as a perfect dielectric drop always deforms to a prolate shape in the presence of a uniform electric field. This prolate deformation causes an asymmetry in shape when the electric field is tilted with respect to the flow direction, leading to cross-stream migration of a perfect dielectric drop.

So far, we have considered the cross-stream migration velocity, but the axial velocity is also of great importance in the context of the trajectory of the drop. Equation (4.4) shows that both charge convection and shape deformation alter the axial drop velocity. The charge-convection-induced alteration in the axial velocity of the drop is due to the presence of an asymmetric charge distribution about the transverse plane, while the deformed shape of the drop leads to a change in the cross-sectional area and charge distribution of the drop, which also leads to change in axial velocity of drop. In figure 8 we show the combined effect of charge convection and shape deformation on U_{dz}. Here we have normalized U_{dz} by the imposed flow velocity at the centre of the drop, which is represented by $|\boldsymbol{V}_\infty|$. In the absence of any externally applied electric field, the drop always lags behind the flow, as the axial velocity of the drop is less than the velocity of the imposed flow at the centre of the drop, as obtained by Chan & Leal (1979) and also shown in figure 8 (solid blue line). With increasing viscosity ratio, the drop becomes much more viscous as compared to the suspending medium,

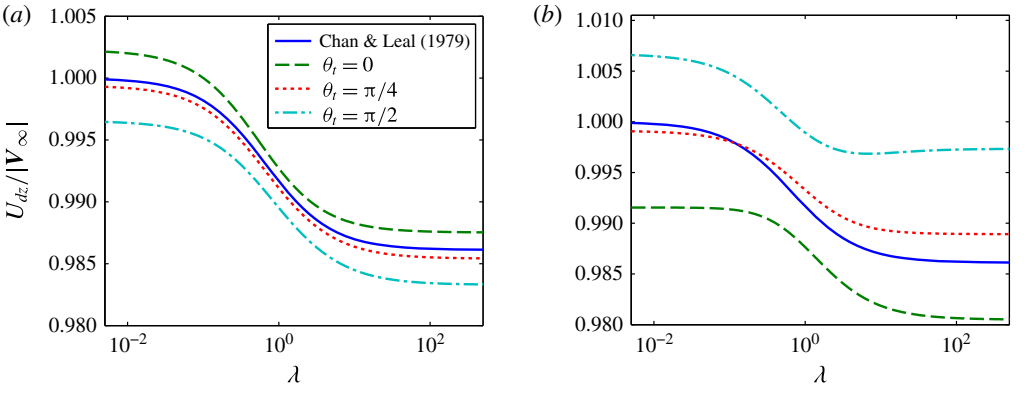

FIGURE 8. (Colour online) Combined effect of charge convection and shape deformation on the normalized axial velocity of the drop ($U_{dz}/|\boldsymbol{V}_\infty|$) with viscosity ratio ($\lambda$) for (*a*) $(R, S) = (5, 0.5)$ and (*b*) $(R, S) = (0.5, 5)$. Other parameters have the following values $Ca = 0.2$, $Re_E = 0.2$, $M = 1$, $\theta_t = \pi/8$, $H = 10$ and $x_d = 4$ (which gives $|\boldsymbol{V}_\infty| = 0.96$).

and moves much more slowly. Figure 8(*a*) shows that application of an electric field has the ability to move the drop much faster (for $\theta_t = 0$) or slower (for $\theta_t = \pi/4$, $\pi/2$) as compared to the case of no electric field. Another interesting fact to note here is that the presence of an electric field can also lead to faster/slower motion of the drop as compared to the flow velocity at the centre of the drop (represented by $U_{dz}/|\boldsymbol{V}_\infty| > 1$). Not only does the tilt angle alter U_{dz} significantly, but also the electrical property ratios (R, S) have a profound effect, as evident from figure 8(*b*). So, depending on the tilt angle (θ_t), electrohydrodynamic property ratios (R, S, λ) and dimensionless numbers (Ca, Re_E, M), the axial velocity of the drop can increase or decrease due to the presence of an electric field.

4.2.2. *Drop trajectory*

Now we investigate the effects of charge convection and shape deformation in terms of different relevant electrohydrodynamic parameters on the quasi-steady-state drop trajectory (represented by (3.31)) and cross-stream migration time scale (represented by (3.33)). First, we plot drop trajectory in plane Poiseuille flow disregarding the effect of the electric field in figure 9(*a*), which has previously obtained by Chan & Leal (1979). For $\lambda = 0.5$, if the drop is placed at some off-centreline location ($x_{d,0} = 4$ or 6), the drop migrates towards the centreline of the flow and the final steady state transverse position of the drop will be the centreline $x_d = H/2 = 5$. If the drop is initially placed at the centreline ($x_{d,0} = 5$), then the drop will move only in the axial direction. Distinctively different drop trajectories are obtained when a tilted uniform electric field is applied in the presence of plane Poiseuille flow, as shown in figure 9(*b*,*c*). In figure 9(*b*) we show the independent effects of charge convection and shape deformation on the drop trajectory when the drop is placed at an off-centreline position ($x_{d,0} = 4$). In the absence of shape deformation ($Ca = 0$), the drop migrates away from the channel centreline solely due to charge convection ($Re_E = 0.1$) because $G_{Re_E} < 0$ (which leads to transverse motion of the drop in the negative x-direction) for $\theta_t = \pi/4$ and the electrical properties under consideration ($R = 5$, $S = 0.5$). In this case we have shown the drop trajectory only for short times, because for longer times the drop moves close to the lower wall, where the effect of the wall in terms of

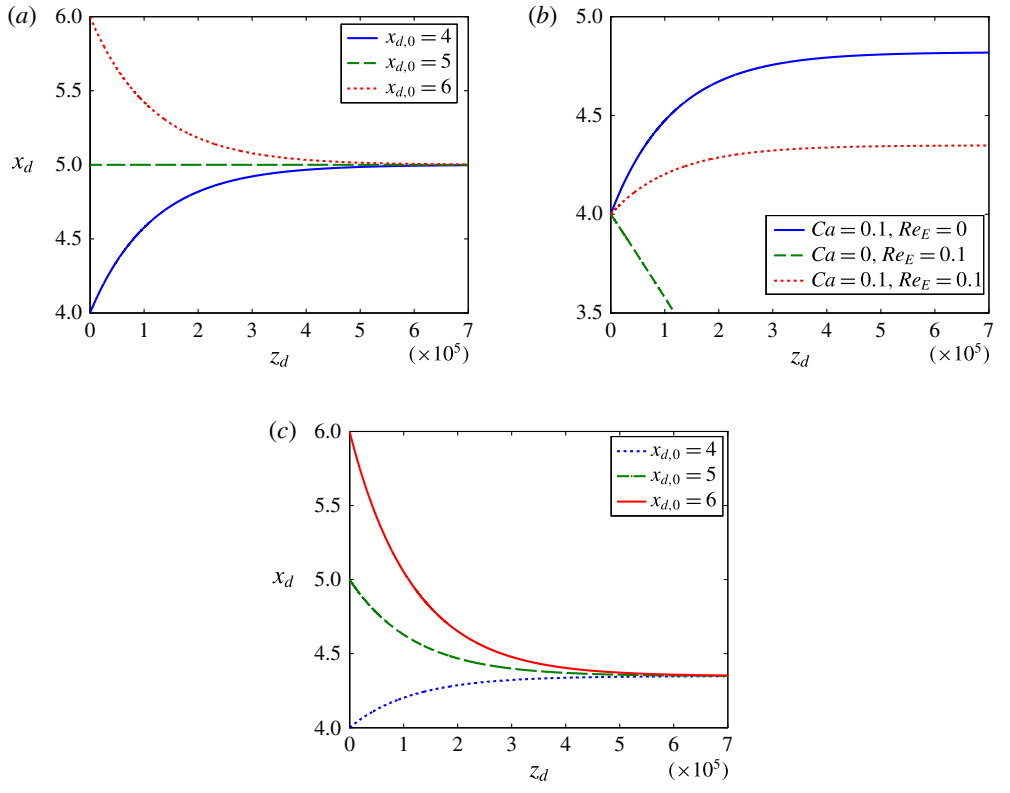

FIGURE 9. (Colour online) (*a*) Drop trajectory in plane Poiseuille flow in the absence of an electric field for different initial transverse position of the drop. Other parameters are used as $Ca = 0.1$, $\lambda = 0.5$, and $H = 10$. (*b*) Drop trajectory in plane Poiseuille flow in the presence of an electric field considering the effect of shape deformation and charge convection separately. Other parameters are used as $M = 0.1$, $\theta_t = \pi/4$, $R = 5$, $S = 0.5$, $\lambda = 0.5$, $H = 10$ and $x_{d,0} = 4$. (*c*) Drop trajectory in plane Poiseuille flow in the presence of an electric field for $x_{d,0} = 4, 5, 6$. Other parameters are taken as $Ca = 0.1$, $Re_E = 0.1$, $M = 0.1$, $\theta_t = \pi/4$, $R = 5$, $S = 0.5$, $\lambda = 0.5$ and $H = 10$.

the hydrodynamic lift force will be significant, which we have not considered in the present analysis. On the other hand, in the absence of charge convection ($Re_E = 0$), the drop migrates towards the centreline solely due to shape deformation ($Ca = 0.1$), but surprisingly the drop does not attain a steady state transverse position at the centreline. This is attributed to the altered shape of the drop, which is very much different in the presence of an electric field. The combined effect of charge convection ($Re_E = 0.1$) and shape deformation ($Ca = 0.1$) on the drop trajectory will add linearly at this order of approximation, and the drop initially moves towards the centreline, but the final steady state transverse position of the drop is distinctly different from the centreline. The drop settles below the centreline, as shown in figure 9(*b*). When the electric field is absent, the drop will always settle to the centreline of the flow irrespective of the initial drop position ($x_{d,0}$) for $\lambda = 0.5$ (as evident from figure 9*a*). In the presence of the electric field, the drop settles to a fixed transverse position irrespective of the initial transverse position of the drop ($x_{d,0}$) for fixed electrohydrodynamic parameters (as evident form figure 9*c*, which considers $x_{d,0} = 4, 5, 6$). But the difference lies in the

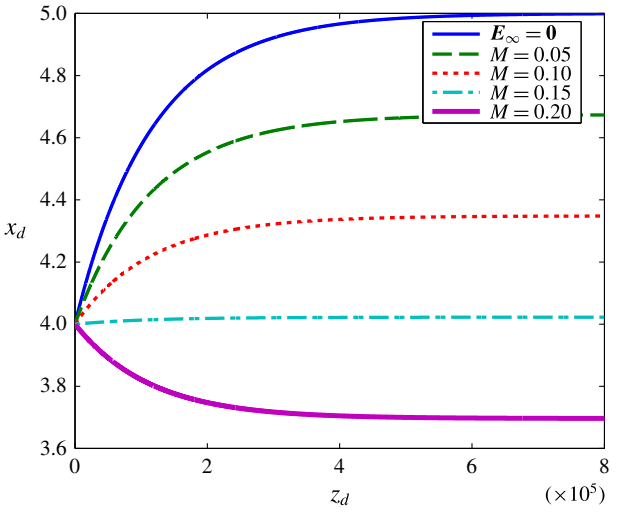

FIGURE 10. (Colour online) Drop trajectory for different values of the Mason number (M). Different parameters are considered as $Ca = 0.1$, $Re_E = 0.1$, $\theta_t = \pi/4$, $R = 5$, $S = 0.5$, $\lambda = 0.5$, $H = 10$ and $x_{d,0} = 4$.

fact that the presence of the electric field may yield the steady state transverse position of the drop at $x_{d,\infty} \neq H/2$. Even when the drop is initially placed at the centreline $x_{d,0} = H/2 = 5$, the drop migrates away from the centreline to a different transverse position at steady state, as shown in figure 9(*c*). This apparently surprising behaviour is due to the fact that, in the presence of a tilted electric field, the charge distribution and drop shape are both asymmetric with respect to the channel centreline, which is otherwise not possible in the absence of the electric field.

Figure 10 depicts the effect of the Mason number (M) on the drop trajectory for the electrohydrodynamic parameters specified in the figure caption. The Mason number physically represents the relative strength of the electrical stress as compared with the hydrodynamic stress. As compared to the case of no electric field (represented by $\boldsymbol{E}_\infty = \boldsymbol{0}$), the drop migrates to different steady state transverse positions for $M > 0$. For smaller values of M(=0.05, 0.1), the drop migrates towards the centreline, but finally settles below the centreline. However, for larger values of M(=0.2), the drop migrates further away from the centreline. Therefore, the increase in Mason number leads to settling of the drop further away from the centreline, which is attributed to the increase in asymmetry in charge distribution and shape deformation. However, there is no noticeable change in the time required for the drop to settle at the steady state transverse position. This is due to the fact that the cross-stream migration time scale (t_m) depends only on the viscosity ratio and capillary number (as evident from (3.33)).

The effect of the relative strength of the components of the electric field (E_x and E_z) are represented by the tilt angle (θ_t). In figure 11 we show the drop trajectory for different θ_t for the electrohydrodynamic parameters specified in the figure caption. When $\theta_t = 0$, $\pi/2$, π, there is no effect of electric field in terms of alteration in cross-stream migration velocity, as evident from (4.5) and also depicted in figure 11. But in the regime $0 < \theta_t < \pi/2$ and $\pi/2 < \theta_t < \pi$, the application of a uniform electric field dramatically alters the drop trajectory. For the electrohydrodynamic properties under consideration, the drop initially starts to move towards the centreline, but settles below

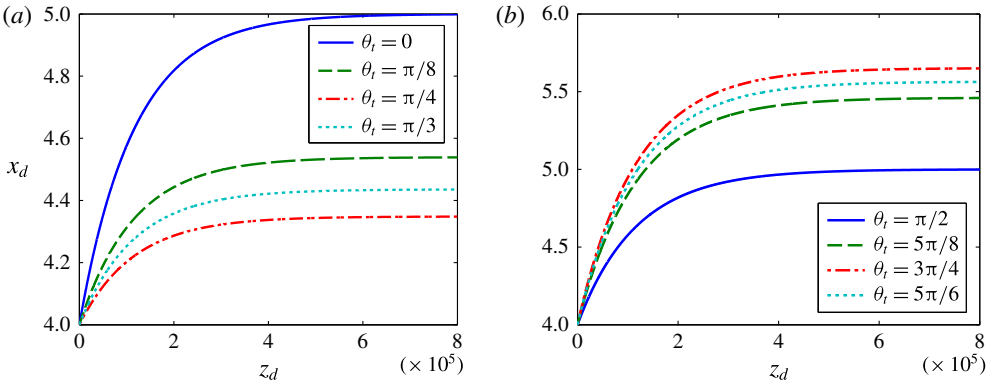

FIGURE 11. (Colour online) Drop trajectory for different tilt angles (θ_t). Different parameters used are $Ca = 0.1$, $Re_E = 0.1$, $M = 0.1$, $R = 5$, $S = 0.5$, $\lambda = 0.5$, $H = 10$ and $x_{d,0} = 4$.

(for $0 < \theta_t < \pi/2$ as depicted in figure 11*a*) or above (for $\pi/2 < \theta_t < \pi$ as depicted in figure 11*b*) the centreline. The effect of tilt angle is most significant near $\theta_t = \pi/4$, $3\pi/4$, as shown in figure 11(*a*,*b*), and the effect of tilt angle reduces for all other values of tilt angle (θ_t).

4.2.3. *Steady state transverse position of the drop*

Figure 12 shows the steady state transverse position of the drop ($x_{d,\infty}$) on the *R*–*S* plane for the parameters mentioned in the figure caption. The colourbar in figure 12 represents the value of the steady state transverse position of the drop ($x_{d,\infty}$). Figure 12(*a*) depicts that, for the combination of small R and large S, $x_{d,\infty} < 5$ (where we have considered the channel height $H = 10$), which represents that the drop settles below the centreline. The drop settles above the centreline ($x_{d,\infty} > 5$) for large R and small S. However, this dependence on (R, S) becomes reversed when $\theta_t = 5\pi/8$ in figure 12(*b*), in which small R and large S lead to settling of the drop above the centreline. An interesting thing to note from figure 12 is that there is a line of $x_{d,\infty} = 5$ which signifies the state of settling of the drop at the centreline. This is associated with the line of zero cross-stream migration velocity ($U_{dx} = 0$) of the drop previously shown in figure 7(*b*).

The pivotal effect of the tilt angle (θ_t) and Mason number (M) on the steady state transverse position of the drop are shown in figure 13 for the parameters specified in the figure caption. We recall (3.32) in the following form

$$x_{d,\infty} = \frac{H}{2}[1 + M \sin(2\theta_t)\Gamma], \tag{4.10}$$

where Γ is a known function of R, S, λ, H, Ca and Re_E that can be easily obtained by comparing (4.10) and (3.32). It is evident from (4.10) that the necessary conditions for $x_{d,\infty} \neq H/2$ are the following: $M \neq 0$ (which means the presence of an electric field) and $\sin(2\theta_t) \neq 0$ (which means a tilted electric field). The sign of the term $\sin(2\theta_t)\Gamma$ is of great importance because this decides whether the drop will settle below or above the centreline. Figure 13(*a*) depicts that, for a particular non-zero magnitude of M, the variation of the steady state transverse position of the drop ($x_{d,\infty}$) is sinusoidal with the tilt angle (θ_t). The drop settles to the centreline $x_{d,\infty} = 5$ (considering $H = 10$)

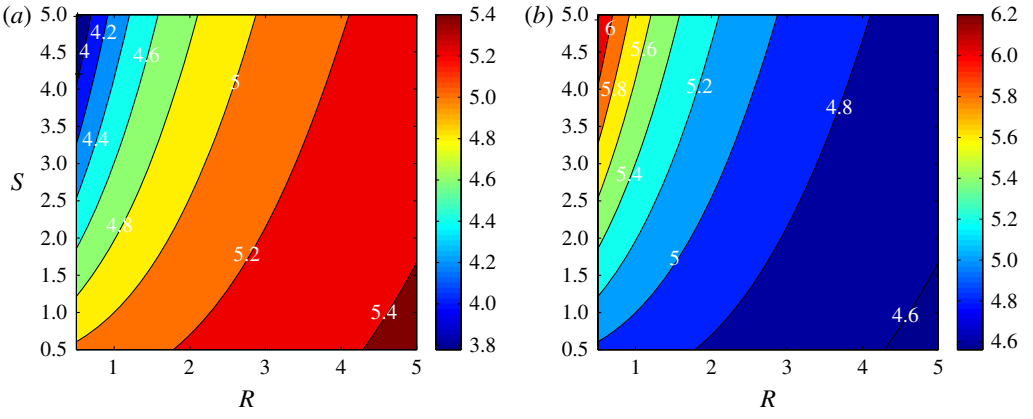

FIGURE 12. (Colour online) Variation of the steady state transverse position of the drop ($x_{d,\infty}$), on the R–S plane for (*a*) $\theta_t = \pi/8$ and (*b*) $\theta_t = 5\pi/8$. Other parameters have the following values: $Ca = 0.1$, $Re_E = 0.1$, $M = 0.1$, $\lambda = 1$, and $H = 10$.

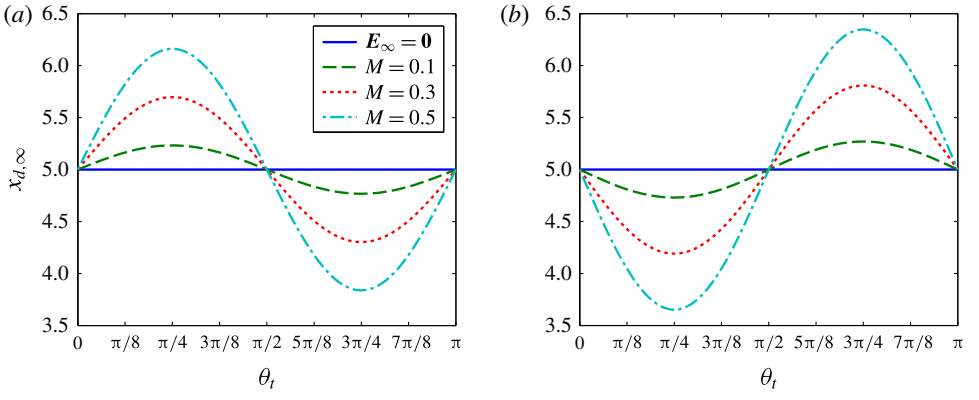

FIGURE 13. (Colour online) Variation of the steady state transverse position of the drop ($x_{d,\infty}$) with the tilt angle (θ_t) for different values of Mason number (M). Electrical property ratios are taken as $(R, S) = (5, 0.5)$ and $(R, S) = (0.5, 1.25)$ to plot (*a*) and (*b*) respectively. Other parameters employed are $Ca = 0.1$, $Re_E = 0.1$, $H = 10$ and $\lambda = 0.25$.

when $\theta_t = 0$, $\pi/2$, π; whereas, for any other values of the tilt angle, the drop settles either above or below the centreline for the parameters under consideration. For figure 13(*a*), $\Gamma > 0$, which gives $\sin(2\theta_t)\Gamma > 0$ for $0 < \theta_t < \pi/2$ and $\sin(2\theta_t)\Gamma < 0$ for $\pi/2 < \theta_t < \pi$. So, for given physical properties we can alter $x_{d,\infty}$ by changing θ_t. One interesting thing to note from figure 13(*a*) is that there is an optimum value of tilt angle ($\theta_t = \pi/4$, $3\pi/4$) for which $|x_{d,\infty} - H/2|$ is maximum and the drop settles far away from the centreline. The reason behind the existence of such an optimum θ_t is that the asymmetry created in the charge distribution and shape deformation due to the presence of the electric field are maximum for $\theta_t = \pi/4$, $3\pi/4$. Next, we plot figure 13(*b*) for $\Gamma < 0$ using the properties mentioned in the figure caption. Here we obtain $\sin(2\theta_t)\Gamma < 0$ for $0 < \theta_t < \pi/2$ and $\sin(2\theta_t)\Gamma > 0$ for $\pi/2 < \theta_t < \pi$. The effect of Mason number on the steady state transverse position of the drop is also depicted in figure 13. With increasing M, the drop moves further away from the

centreline. This is attributed to the fact that the increase in M results in an increase of the relative magnitude of the electrical stress as compared to viscous stresses, which brings about the change in flow field, and finally the drag force on the drop. Accordingly, M only controls the strength of alteration in drop motion due to an electric field, whereas the tilt angle θ_t has the ability to affect the direction in which the drop settles with respect to the centreline.

4.3. *Comparison of the analytical solution against numerical simulations*

4.3.1. *Numerical method and simulation set-up*

Two-phase electrohydrodynamic simulations are performed using the open-source scientific package GERRIS (http://gfs.sf.net) developed by Popinet (2003, 2009), which employs the volume-of-fluid (VOF) method in a finite-volume framework. The choice of GERRIS is made because the ELECTROHYDRO module (López-Herrera, Popinet & Herrada 2011) of GERRIS solves the incompressible Navier–Stokes equation coupled with an electric potential and electric charge density very accurately (Ferrera *et al.* 2013; Cimpeanu, Papageorgiou & Petropoulos 2014; Datta, Das & Das 2015; López-Herrera *et al.* 2015). Another important factor is that GERRIS is equipped with dynamic adaptive mesh refinement, which allows one to use a greater number of computational cells near the desired regions dynamically (Popinet 2003). This is very advantageous in the present simulations because we have to use a very long channel to simulate the drop motion towards steady state. The electric potential (ψ) satisfies the Poisson equation and the electric charge density (q_v) satisfies the charge conservation equation of the following form (López-Herrera *et al.* 2011)

$$\left.\begin{gathered}\boldsymbol{\nabla}\cdot(\varepsilon\boldsymbol{\nabla}\psi) = -q_v,\\ Re_E\left[\frac{\partial q_v}{\partial t} + \boldsymbol{\nabla}\cdot(q_v\boldsymbol{u})\right] = \boldsymbol{\nabla}\cdot(\sigma\boldsymbol{\nabla}\psi).\end{gathered}\right\} \tag{4.11}$$

The right-hand side of the charge transport equation $\boldsymbol{\nabla}\cdot(\sigma\boldsymbol{\nabla}\psi)$ is the Ohmic current, which is the equivalent of the electromigration term in electrokinetic theory (Saville 1997). This is obtained by noting that the conservation of the volumetric charge density may be written as (Saville 1997) $\partial q_v/\partial t + \boldsymbol{u}\cdot\boldsymbol{\nabla}q_v = \boldsymbol{\nabla}\cdot[\sum_k \omega^k e^2 z^k n^k \boldsymbol{\nabla}\psi + \omega^k k_B T \boldsymbol{\nabla} q_v]$, $k = 1, 2, \ldots, N$, where ω^k represents the mobility of the kth species, n^k is the ionic concentration of the kth species, e is the charge of a proton, k_B is the Boltzmann constant and T is the absolute temperature. In the limit where the charge diffusion is negligible, the description may be reduced simply as (4.11). It is important to note here that GERRIS solves for the charge density (q_v) in the bulk fluid. However, as the charge-relaxation time scale is very small as compared to the convective time scale (represented by small value of Re_E), the charges which are present at the bulk fluid will be accumulated at the fluid–fluid interface very quickly (López-Herrera *et al.* 2011; Ferrera *et al.* 2013). So, we can expect that (4.11) will effectively represent the bulk fluid as charge-free, and the charge conservation equation in the bulk will be the same as the charge conservation equation at the interface (represented in boundary condition *e*4). Fluid flow is governed by the continuity equation and the Navier–Stokes equation of the form (López-Herrera *et al.* 2011)

$$\left.\begin{gathered}\boldsymbol{\nabla}\cdot\boldsymbol{u} = 0,\\ Re\left(\frac{\partial \boldsymbol{u}}{\partial t} + \boldsymbol{u}\cdot\boldsymbol{\nabla}\boldsymbol{u}\right) = -\boldsymbol{\nabla}p + \boldsymbol{\nabla}\cdot[\mu\{\boldsymbol{\nabla}\boldsymbol{u} + (\boldsymbol{\nabla}\boldsymbol{u})^{\mathrm{T}}\}] + M\boldsymbol{F}^e + \frac{1}{Ca}\boldsymbol{F}_s,\end{gathered}\right\} \tag{4.12}$$

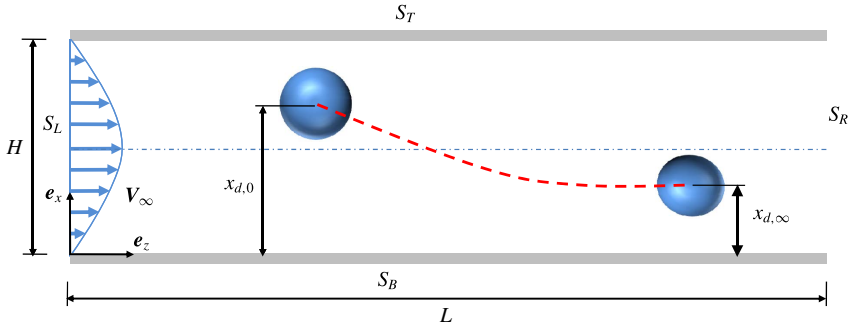

FIGURE 14. (Colour online) Schematic representation of the simulation set-up. 2D rectangular domian of length L and height H is considered which is bounded by the inlet left boundary (S_L), the outlet right boundary (S_R), and the top and bottom walls (S_T, S_B). The drop is initially placed at some transverse position $x_{d,0}$. The steady state transverse position ($x_{d,\infty}$), is obtained from the simulation data.

where $Re = \rho_e V_c a/\mu_e$ is the Reynolds number. The electric force density ($\boldsymbol{F}_e$) and surface tension force ($\boldsymbol{F}_s$) are implemented in GERRIS as volume forces by López-Herrera *et al.* (2011). The electric force density is related to the electric field ($\boldsymbol{E}$) and the charge density (q_v) as $\boldsymbol{F}_e = q_v\boldsymbol{E} - (1/2)|\boldsymbol{E}|^2\nabla\varepsilon$. The surface tension force is related to the radius of curvature of the interface (κ) as $\boldsymbol{F}_s = \kappa\delta_s\boldsymbol{n}$, where δ_s is the Dirac delta function and $\boldsymbol{n}$ is the unit normal vector on the drop interface. GERRIS implements the volume-of-fluid (VOF) method to capture the fluid–fluid interface. The volume fraction (c) satisfies an advection equation of the form

$$\frac{\partial c}{\partial t} + \nabla\cdot(c\boldsymbol{u}) = 0. \tag{4.13}$$

The drop phase is represented by $c = 1$, whereas the suspending medium is represented by $c = 0$. Variation of all the electrohydrodynamic properties across the drop interface is expressed in terms of the following weighted arithmetic interpolation (López-Herrera *et al.* 2011): $\mu = c\lambda + (1-c)$, $\varepsilon = cS + (1-c)$ and $\sigma = cR + (1-c)$.

To simulate the electrohydrodynamic motion of the drop, we consider a two-dimensional (2D) rectangular domain of dimensionless length L and dimensionless height H (refer to figure 14). We consider $H = 4$ and $L = 180$ to simulate the drop dynamics. The choice of a relatively small domain height of $H = 4$ is based on the fact that a larger channel height requires a very large length of channel to get steady state drop velocity. This large computational domain is associated with a large computational time. As the electric potential varies in both the axial and transverse directions, the periodic boundary condition is not applicable in the present set-up. We need to use a full length domain to simulate the drop dynamics until the steady state is reached. To reduce the excessively large length of the computational domain and reduce the computational time, we have taken $H = 4$. The whole computational domain is composed of 45 square boxes of size $H = 4$. All the boxes are decomposed using square surface elements with cell size in the bulk fluid as $H/8$. In the present study, we have used a gradient-based adaptive mesh refinement (Popinet 2003) in which the computational cells are divided with quadtree discretization where the gradient in volume fraction is present. The cell size near the drop interface is $H/256$, which is equivalent to 64 grid points over the drop radius. Recent studies have

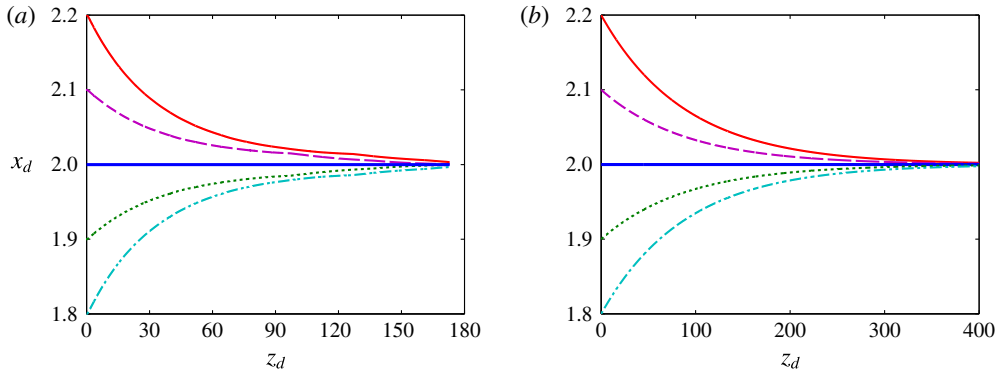

FIGURE 15. (Colour online) (*a*) Numerically obtained drop trajectories in plane Poiseuille flow in the absence of an electric field for different initial transverse positions of the drop. (*b*) Analytically obtained drop trajectories in plane Poiseuille flow in the absence of an electric field for different initial transverse positions of the drop. Other parameters have the following values: $Ca = 0.2$, $\lambda = 0.1$ and $H = 4$. For the numerical simulations, we have considered $Re = 0.1$.

employed a similar grid size to simulate drop electrohydrodynamics using GERRIS (López-Herrera *et al.* 2011; Ferrera *et al.* 2013; Chen *et al.* 2015) and found excellent agreement with existing results. We apply the following boundary conditions for the electric potential and the velocity field in the respective domain boundaries:

$$\left.\begin{gathered}\psi|_{S_L} = E_z L + E_x H\left(1 - \frac{x}{H}\right), \quad \psi|_{S_R} = E_x H\left(1 - \frac{x}{H}\right), \\ \psi|_{S_B} = E_x H + E_z(L - z), \quad \psi|_{S_T} = E_x H + E_z(L - z), \\ \boldsymbol{u}|_{S_L} = \boldsymbol{u}|_{S_R} = \frac{4x}{H}\left(1 - \frac{x}{H}\right), \quad \boldsymbol{u}|_{S_T} = \boldsymbol{u}|_{S_B} = \boldsymbol{0}.\end{gathered}\right\} \tag{4.14}$$

The initial velocity field throughout the domain is considered as plane Poiseuille flow. The drop is placed initially at an axial location $z_{d,0} = 3H/2$ so that drop is not affected by the inlet boundary (S_L). The initial transverse position of the drop ($x_{d,0}$) is taken very close to the channel centreline to minimize the wall effects. While showing the drop trajectories, the axial location at any time t, $z_d(t)$, is expressed as $z_d(t) - z_{d,0}$. We have validated the numerical code in the following two cases: (i) drop trajectory in Poiseuille flow and (ii) drop deformation in a uniform electric field. We have also performed grid independence study considering the combined effect of a tilted electric field and Poiseuille flow. Details regarding model validation and grid independence are presented in appendix H.

4.3.2. *Drop trajectory*

Now, we show the drop trajectory, $z_d(t) - x_d(t)$, obtained from 2D numerical computations and compare that with the analytical solution. Figure 15(*a*) depicts the drop trajectory in Poiseuille flow in the absence of an electric field for the parameters mentioned in the figure caption. Chan & Leal (1979) have shown analytically that for $\lambda = 0.1$ the drop settles to the centreline. The present analytical solution in the limit of $\boldsymbol{E}_\infty = \boldsymbol{0}$ yields the same result as that of Chan & Leal (1979), which is depicted in figure 15(*b*). The present numerical computations show that the drop settles to

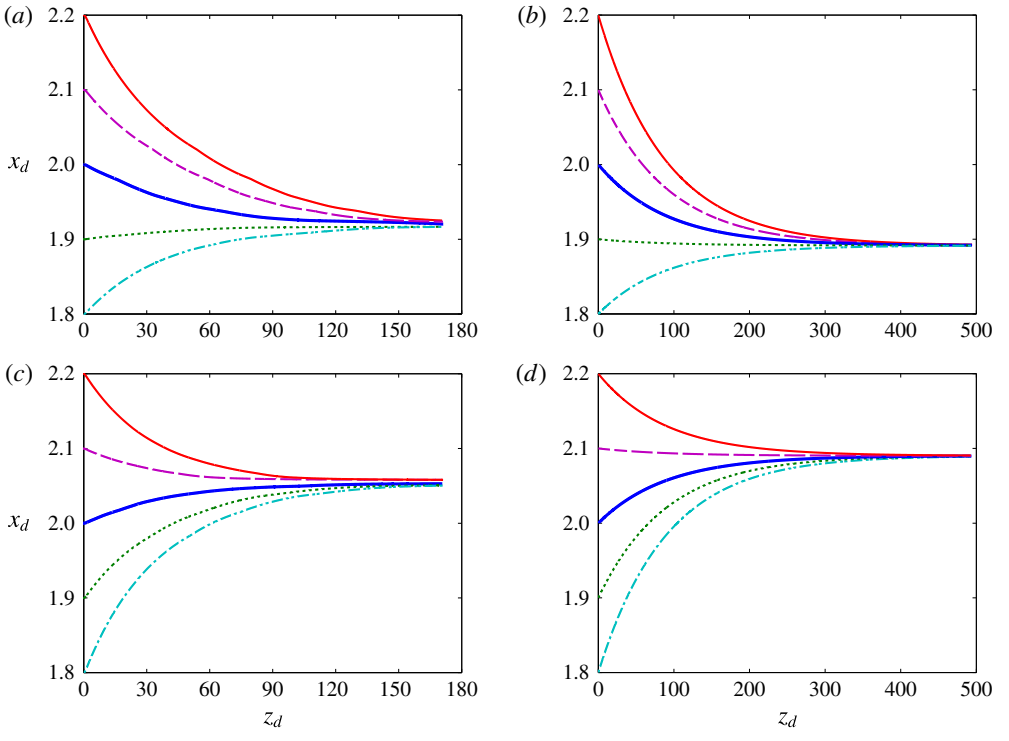

FIGURE 16. (Colour online) (*a*) Numerically obtained drop trajectory in plane Poiseuille flow in the presence of a tilted electric field ($\theta_t = 5\pi/16$) for $R = 0.75$. (*b*) Analytically obtained drop trajectory in plane Poiseuille flow in the presence of a tilted electric field ($\theta_t = 5\pi/16$) for $R = 0.75$. (*c*) Numerically obtained drop trajectory in plane Poiseuille flow in the presence of a tilted electric field ($\theta_t = \pi/4$) for $R = 1.25$. (*d*) Analytically obtained drop trajectory in plane Poiseuille flow in the presence of a tilted electric field ($\theta_t = \pi/4$) for $R = 1.25$. Other parameters have the following values: $S = 1$, $Ca = 0.2$, $Re_E = 0.2$, $\lambda = 0.1$ and $H = 4$. Numerical simulations we performed for $Re = 0.1$.

the centreline for different initial transverse positions ($x_{d,0}$). Though the steady state transverse position from numerical and analytical solutions show the exact same result (i.e. $x_{d,\infty} = H/2 = 2$), the numerically obtained axial length traversed by the drop differs significantly from the analytical solution. This difference is attributed to the presence of the bounding walls and the associated hydrodynamic lift force acting on the drop (Chan & Leal 1979; Uijttewaal *et al.* 1993; Uijttewaal & Nijhof 1995). As we have performed our numerical simulation considering the channel height $H = 4$, the wall effects are not negligible.

The effect of a tilted electric field is shown in figure 16 for the parameters mentioned in the figure caption. Figures 16(*a*) and 16(*b*) are obtained for $R = 0.75$ and $\theta_t = 5\pi/16$, while figures 16(*c*) and 16(*d*) are obtained for $R = 1.25$ and $\theta_t = \pi/4$. Figures 16(*a*) and 16(*c*) are obtained from numerical simulations, while figures 16(*b*) and 16(*d*) are obtained from analytical solutions. Two important things to note from figure 16(*a*) are as follows: first, in the presence of a tilted electric field, the charge convection and shape deformation lead to settling of the drop below the centreline. Second, the off-centreline steady state transverse position ($x_{d,\infty}$) is independent of the initial transverse position ($x_{d,0}$). For all $x_{d,0}$ values we obtain

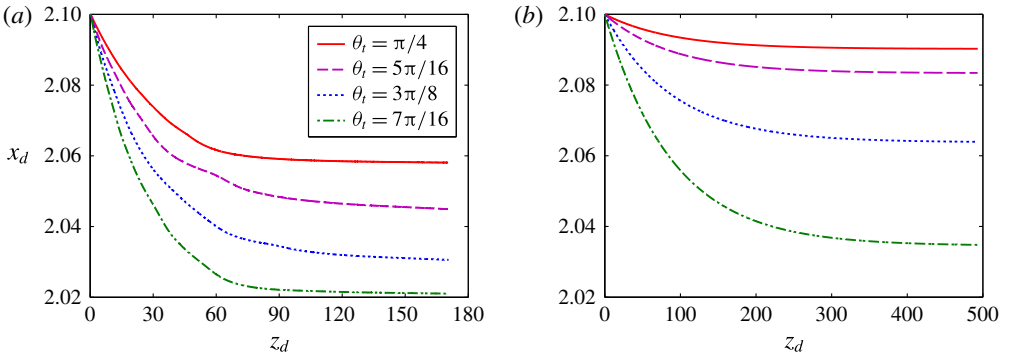

FIGURE 17. (Colour online) (*a*) Numerically obtained drop trajectory in plane Poiseuille flow in the presence of a tilted electric field for different tilt angles. (*b*) Analytically obtained drop trajectory in plane Poiseuille flow in the presence of a tilted electric field for different tilt angles. Different parameters are taken as $Ca = 0.2$, $Re_E = 0.2$, $R = 1.25$, $S = 1$, $\lambda = 0.1$ and $H = 4$. Numerical simulations were performed for $Re = 0.1$.

nearly equal values of $x_{d,\infty}$. This is true even when the drop is initially placed at the centreline (i.e. $x_{d,0} = H/2 = 2$). Figure 16(*b*) depicts the drop trajectory for the same parameters obtained from the analytical solution. Comparison between the analytical and numerical solutions reveals that both methods qualitatively represent similar results. Similar qualitative agreement between the numerical and analytical solutions is also depicted in figures 16(*c*) and 16(*d*), in which the drop settles above the centreline.

To investigate the effect of tilt angle on the drop trajectory and steady state transverse position of the drop, we plot the drop trajectory for the following four different values of $\theta_t = \pi/4$, $5\pi/16$, $3\pi/8$ and $7\pi/16$, while the other parameters are mentioned in the figure caption. Figure 17(*a*) depicts the numerically obtained drop trajectories. Numerical simulations show that the drop settles away from the flow centreline for $\theta_t = \pi/4$. With increasing tilt angle, the drop still settles in an off-centreline transverse position, but the drop settles much closer to the centreline. This is due to the fact that the asymmetry in charge distribution and shape deformation are larger for $\theta_t = \pi/4$. Analytical solutions depicted in figure 17(*b*) compare qualitatively well with the numerical simulations.

Possible reasons for the lack of an exact match between the analytical and numerical solutions are the presence of bounding walls and a 2D domain. Bounding walls in the presence of drop deformation lead to a hydrodynamic lift force on the drop towards the centreline (Chan & Leal 1979; Uijttewaal *et al.* 1993; Uijttewaal & Nijhof 1995), which facilitates faster migration of the drop. That is why the numerically obtained drop trajectories show relatively faster settling of the drop to the steady state transverse position as compared to the analytically obtained drop trajectories. This effect is present even in the absence of an electric field (refer to figure 15*a*). Another way in which bounding wall affects the drop motion is the non-uniformity and asymmetry in an electric field due to the positioning of drop at an off-centreline location (Halim & Esmaeeli 2013; Esmaeeli 2016). In the present study, we have restricted ourselves to a 2D domain to reduce computational cost. A three-dimensional (3D) numerical simulation, which is expected to compare better with the analytical solution, is considered as a future study.

5. Conclusions

5.1. *Summary of the findings*

In this paper, we have studied the electrohydrodynamic motion of a Newtonian, leaky dielectric drop in a plane Poiseuille flow in the presence of a uniform electric field. Considering the combined effect of surface charge convection at the drop surface and shape deformation, we obtain $O(Re_E)$ and $O(Ca)$ corrections to the drop velocity by performing a double asymptotic expansion in terms of the electric Reynolds number (Re_E) and capillary number (Ca) as the perturbation parameters. The important conclusions that can be drawn from the present study are the following.

(i) Application of a uniform electric field modulates the mechanism of cross-stream migration dramatically via charge convection and shape deformation. However, the presence of an electric field is not a sufficient condition for the alteration in cross-stream migration velocity of the drop. We obtain that the electric field affects the cross-stream migration of the drop if the applied electric field is tilted with respect to the imposed flow direction, which necessitates the following condition to be satisfied by the tilt angle: $0 < \theta_t < \pi/2$ or $\pi/2 < \theta_t < \pi$.

(ii) We find a new source of cross-stream migration of the drop in plane Poiseuille flow. In the presence of a tilted electric field, the charge distribution at the drop surface becomes asymmetric due to charge convection, which finally yields a cross-stream migration velocity of the drop ($U_{dx}^{(Re_E)}$). This component of cross-stream migration is present even for a non-deformable spherical drop. We obtain the direction of cross-stream migration of the drop due to charge convection as: depending on the sign of the term $G_{Re_E} = E_x E_z (S - R)(3R - S + 3)$, the drop can migrate in the positive x-direction ($U_{dx}^{(Re_E)} > 0$) for $G_{Re_E} > 0$ and the reverse happens ($U_{dx}^{(Re_E)} < 0$) for $G_{Re_E} < 0$.

(iii) When the electric field is absent, the shape of a drop in a plane Poiseuille flow becomes asymmetric with respect to the channel centreline if the drop is placed at some off-centreline location, thereby leading to migration of the drop towards or away from the channel centreline depending on the viscosity ratio (λ), as shown by Chan & Leal (1979). In the presence of the electric field, the drop deforms also due to generation of Maxwell stresses at the drop interface. If the applied electric field is tilted, then it alters the asymmetry in drop shape, which further modifies the drop velocity in both the axial and cross-stream directions.

(iv) Depending on the magnitude of the controlling parameters, combined effects of charge convection and shape deformation not only increase/decrease the drop velocity but also lead to cross-stream motion of the drop in the reverse direction as compared to the case of no electric field.

(v) At steady state, the drop can settle either at the centreline or below/above the centreline, depending on the tilt angle (θ_t), Mason numbers (M), capillary number (Ca), electric Reynolds number (Re_E) and the electrohydrodynamic property ratios (R, S, λ). Interestingly, the steady state transverse position of the drop is independent of the initial transverse position of the drop. Hence, a drop initially placed at the centre of the plane Poiseuille flow can migrate away from the centreline due to charge convection and shape deformation.

(vi) Direct comparison of analytical solution with the 2D numerical simulation shows qualitative agreement in predicting the drop trajectory. Numerical simulation shows faster motion of the drop as compared with the analytically obtained drop velocity. The lack in quantitative agreement might be due to the 2D

simulation domain and the presence of bounding walls. Bounding walls induce a hydrodynamic lift force on the deformed drop towards the centreline, which leads to faster cross-stream motion of the drop in the numerical simulations.

5.2. *Remarks*

The above analytical and numerical studies facilitate us to acquire an idea about the various controlling parameters which affect the drop velocity, drop trajectory and steady state transverse position of the drop in the presence of a uniform electric field and background plane Poiseuille flow field. Using these, we may achieve fine-tuned control over the motion and final steady transverse position of drops in droplet-based microfluidic devices. The cross-stream migration of drops, which is governed by the direction of the applied electric field and the electrical properties, may also be employed for sorting of drops. Though the validity of the present analytical model relies on the fact that Ca and Re_E should be much smaller than unity, we believe that this perturbation analysis brings out the important physical mechanisms that are directly involved in cross-stream migration of the drop. In the present study, we have focused only on the effect of curvature on the drop migration characteristics by neglecting the effects of bounding walls. Both electric and flow fields are expected to be affected by the presence of bounding walls, which in turn may alter the drop migration velocity. We believe that a study of wall effects on the flow field and electric field distribution and its consequence on the drop velocity can be targeted as potential future work. While the present 2D numerical simulations include the wall effects and compare only qualitatively with the analytical model, a full 3D numerical simulation could be of great value towards simulating the drop electrohydrodynamics in practical microfluidic platforms; this is being pursued by the authors.

Acknowledgements

A.B. and S.C. would like to acknowledge funding from SRIC, IIT Kharagpur under the Project 'Centre of Excellence for Training and Research in Microfluidics'. The authors would like to acknowledge the whole GERRIS FLOW SOLVER community (http://gfs.sf.net) for making such a wonderful free software program. S.M. is grateful to Mr S. Datta for valuable discussions regarding numerical computations in GERRIS.

Supplementary material

Supplementary material is available at https://doi.org/10.1017/jfm.2016.677.

Appendix A. Expression for the solid harmonics present in the velocity and pressure fields at leading order

The velocity and pressure fields (3.9) and (3.10) inside the drop consist of the following growing solid harmonics

$$\left.\begin{gathered}\chi_1^{(0)} = r\hat{C}_{1,1}^{(0)} \sin\phi P_{1,1}, \quad \chi_2^{(0)} = r^2\hat{C}_{2,2}^{(0)} \sin(2\phi) P_{2,2}, \\ \Phi_1^{(0)} = rB_{1,0}^{(0)} P_{1,0}, \quad \Phi_2^{(0)} = r^2[B_{2,0}^{(0)} P_{2,0} + B_{2,1}^{(0)} \cos\phi P_{2,1} + B_{2,2}^{(0)} \cos(2\phi) P_{2,2}], \\ \Phi_3^{(0)} = r^3[B_{3,0}^{(0)} P_{3,0} + B_{3,2}^{(0)} \cos(2\phi) P_{3,2}], \quad p_1^{(0)} = \lambda r A_{1,0}^{(0)} P_{1,0}, \\ p_2^{(0)} = \lambda r^2[A_{2,0}^{(0)} P_{2,0} + A_{2,1}^{(0)} \cos\phi P_{2,1} + A_{2,2}^{(0)} \cos(2\phi) P_{2,2}], \\ p_3^{(0)} = \lambda r^3[A_{3,0}^{(0)} P_{3,0} + A_{3,2}^{(0)} \cos(2\phi) P_{3,2}],\end{gathered}\right\} \tag{A 1}$$

where the unknown coefficients are obtained as

$$\left.\begin{gathered}
A_{1,0}^{(0)}=\frac{10k_2}{2+3\lambda},\quad A_{2,0}^{(0)}=-\frac{63}{10}(E_x^2-2E_z^2)\Lambda,\quad A_{2,1}^{(0)}=\frac{7k_1}{2(1+\lambda)}+\frac{63}{5}E_xE_z\Lambda,\\
A_{2,2}^{(0)}=\frac{63}{20}E_x^2\Lambda,\quad A_{3,0}^{(0)}=-\frac{3k_2}{1+\lambda},\quad A_{3,2}^{(0)}=\frac{k_2}{2(1+\lambda)},\quad B_{1,0}^{(0)}=-\frac{A_{1,0}^{(0)}}{10},\\
B_{2,0}^{(0)}=-\frac{A_{2,0}^{(0)}}{14},\quad B_{2,1}^{(0)}=-\frac{A_{2,1}^{(0)}}{14},\quad B_{2,2}^{(0)}=-\frac{A_{2,2}^{(0)}}{14}\quad B_{3,0}^{(0)}=-\frac{A_{3,0}^{(0)}}{18},\quad B_{3,2}^{(0)}=-\frac{A_{3,2}^{(0)}}{18},\\
\hat{C}_{1,1}^{(0)}=-\frac{k_1}{2},\quad \hat{C}_{2,2}^{(0)}=-\frac{5k_2}{18(4+\lambda)},
\end{gathered}\right\}\tag{A 2}$$

where $\Lambda=(M(R-S))/((\lambda+1)(R+2)^2)$. The velocity and pressure fields (3.11) and (3.12) outside the drop consist of the following growing solid harmonics

$$\left.\begin{gathered}
\chi_{-3}^{(0)}=\frac{1}{r^3}\hat{C}_{-3,2}^{(0)}\sin(2\phi)P_{2,2},\quad \Phi_{-2}^{(0)}=\frac{1}{r^2}B_{-2,0}^{(0)}P_{1,0},\\
\Phi_{-3}^{(0)}=\frac{1}{r^3}[B_{-3,0}^{(0)}P_{2,0}+B_{-3,1}^{(0)}\cos\phi P_{2,1}+B_{-3,2}^{(0)}\cos(2\phi)P_{2,2}],\\
\Phi_{-4}^{(0)}=\frac{1}{r^4}[B_{-4,0}^{(0)}P_{3,0}+B_{-4,2}^{(0)}\cos(2\phi)P_{3,2}],\\
p_{-2}^{(0)}=\frac{1}{r^2}[A_{-2,0}^{(0)}P_{1,0}+A_{-2,1}^{(0)}\cos\phi P_{1,1}+\hat{A}_{-2,1}^{(0)}\sin\phi P_{1,1}],\\
p_{-3}^{(0)}=\frac{1}{r^3}[A_{-3,0}^{(0)}P_{2,0}+A_{-3,1}^{(0)}\cos\phi P_{2,1}+A_{-3,2}^{(0)}\cos(2\phi)P_{2,2}],\\
p_{-4}^{(0)}=\frac{1}{r^4}[A_{-4,0}^{(0)}P_{3,0}+A_{-4,2}^{(0)}\cos(2\phi)P_{3,2}],
\end{gathered}\right\}\tag{A 3}$$

where the unknown coefficients are obtained as

$$\left.\begin{gathered}
A_{-2,0}^{(0)}=\frac{(2+3\lambda)(U_{dz}^{(0)}-k_0)-\lambda k_2}{2(1+\lambda)},\quad A_{-2,1}^{(0)}=\frac{(2+3\lambda)U_{dx}^{(0)}}{2(1+\lambda)},\quad \hat{A}_{-2,1}^{(0)}=\frac{(2+3\lambda)U_{dy}^{(0)}}{2(1+\lambda)},\\
A_{-3,0}^{(0)}=-\frac{9}{5}(E_x^2-2E_z^2)\Lambda,\quad A_{-3,1}^{(0)}=-\frac{(2+5\lambda)k_1}{3(1+\lambda)}+\frac{18}{5}E_xE_z\Lambda,\quad A_{-3,2}^{(0)}=\frac{9}{10}E_x^2\Lambda\\
A_{-4,0}^{(0)}=\frac{(2+7\lambda)k_2}{4(1+\lambda)},\quad A_{-4,2}^{(0)}=-\frac{(2+7\lambda)k_2}{24(1+\lambda)},\quad B_{-2,0}^{(0)}=\frac{(1-\lambda)k_2}{5(2+3\lambda)},\quad B_{-3,0}^{(0)}=\frac{A_{-3,0}^{(0)}}{6},\\
B_{-3,1}^{(0)}=-\frac{\lambda k_1}{6(1+\lambda)}+\frac{3}{5}E_xE_z\Lambda,\quad B_{-3,2}^{(0)}=\frac{3}{20}E_x^2\Lambda,\quad B_{-4,0}^{(0)}=\frac{\lambda k_2}{8(1+\lambda)},\\
B_{-4,2}^{(0)}=-\frac{\lambda k_2}{48(1+\lambda)},\quad \hat{C}_{-3,2}^{(0)}=-\frac{(1-\lambda)k_2}{18(4+\lambda)}.
\end{gathered}\right\}\tag{A 4}$$

Appendix B. Expressions for $Z_{n,m}$ present in (3.20)

The non-zero $Z_{n,m}$ terms present in (3.20) are obtained as

$$\left.\begin{gathered}
Z_{1,0}=\frac{3}{50}\frac{(R-S)}{(R+2)^3(\lambda+1)}[\{E_z(R+2)^2(25\lambda+40)\}k_1+36M(R-S)E_z(E_x^2+E_z^2)],\\
Z_{1,1}=-\frac{3}{50}\frac{(R-S)}{(R+2)^3(\lambda+1)}[\{E_z(R+2)^2(25\lambda+40)\}k_1-36M(R-S)E_x(E_x^2+E_z^2)],\\
Z_{2,0}=\frac{6}{7}\frac{E_zk_2(R-S)(4\lambda+5)}{(3\lambda+2)(\lambda+1)(R+2)},\quad Z_{2,1}=\frac{2}{7}\frac{E_x(R-S)k_2(36\lambda^2+119\lambda+75)}{(3\lambda+2)(\lambda+1)(4+\lambda)(R+2)},\\
Z_{2,2}=-\frac{5}{7}\frac{E_zk_2(R-S)(1+2\lambda)}{(4+\lambda)(\lambda+1)(R+2)},\quad Z_{3,3}=\frac{9}{25}\frac{M(R-S)^2E_x^3}{(R+2)^3(\lambda+1)},\\
Z_{3,0}=-\frac{12}{25}\frac{(R-S)[5E_x(R+2)^2k_1+9M(R-S)(3E_x^2-2E_z^2)E_z]}{(\lambda+1)(R+2)^3},\\
Z_{3,1}=\frac{2}{25}\frac{(R-S)[20E_z(R+2)^2k_1+27M(R-S)E_x(-E_x^2+4E_z^2)]}{(\lambda+1)(R+2)^3},\\
Z_{3,2}=\frac{2}{25}\frac{(R-S)[5E_x(R+2)^2k_1+27M(R-S)E_x^2E_z]}{(\lambda+1)(R+2)^3},\quad Z_{4,0}=-\frac{15}{7}\frac{k_2(R-S)E_z}{(\lambda+1)(R+2)},\\
Z_{4,1}=-\frac{45}{56}\frac{(R-S)k_2E_x}{(\lambda+1)(R+2)},\quad Z_{4,2}=\frac{5}{28}\frac{(R-S)k_2E_z}{(\lambda+1)(R+2)},\quad Z_{4,3}=\frac{5}{112}\frac{(R-S)k_2E_x}{(\lambda+1)(R+2)}.
\end{gathered}\right\}\tag{B 1}$$

Appendix C. Expressions for the unknown coefficients of the $O(Re_E)$ electric potential

The unknown coefficients present in the $O(Re_E)$ electric potential (3.21) are obtained in terms of $Z_{n,m}$ in the following form

$$\left.\begin{gathered}
a_{1,0}^{(1)}=\frac{Z_{1,0}}{2+R},\quad a_{1,1}^{(1)}=\frac{Z_{1,1}}{2+R},\quad a_{2,0}^{(1)}=\frac{Z_{2,0}}{3+2R},\quad a_{2,1}^{(1)}=\frac{Z_{2,1}}{3+2R},\quad a_{2,2}^{(1)}=\frac{Z_{2,2}}{3+2R},\\
a_{3,0}^{(1)}=\frac{Z_{3,0}}{4+3R},\quad a_{3,1}^{(1)}=\frac{Z_{3,1}}{4+3R},\quad a_{3,2}^{(1)}=\frac{Z_{3,2}}{4+3R},\quad a_{3,3}^{(1)}=\frac{Z_{3,3}}{4+3R},\quad a_{4,0}^{(1)}=\frac{Z_{4,0}}{5+4R},\\
a_{4,1}^{(1)}=\frac{Z_{4,1}}{5+4R},\quad a_{4,2}^{(1)}=\frac{Z_{4,2}}{5+4R},\quad a_{4,3}^{(1)}=\frac{Z_{4,3}}{5+4R},\quad b_{-2,0}^{(1)}=a_{1,0}^{(1)},\quad b_{-2,1}^{(1)}=a_{1,1}^{(1)},\\
b_{-3,0}^{(1)}=a_{2,0}^{(1)},\quad b_{-3,1}^{(1)}=a_{2,1}^{(1)},\quad b_{-3,2}^{(1)}=a_{2,2}^{(1)},\quad b_{-4,0}^{(1)}=a_{3,0}^{(1)},\quad b_{-4,1}^{(1)}=a_{3,1}^{(1)},\quad b_{-4,2}^{(1)}=a_{3,2}^{(1)},\\
b_{-4,3}^{(1)}=a_{3,3}^{(1)},\quad b_{-5,0}^{(1)}=a_{4,0}^{(1)},\quad b_{-5,1}^{(1)}=a_{4,1}^{(1)},\quad b_{-5,2}^{(1)}=a_{4,2}^{(1)},\quad b_{-5,3}^{(1)}=a_{4,3}^{(1)}.
\end{gathered}\right\}\tag{C 1}$$

Appendix D. Expressions for the coefficients present in $p_{-2}^{(Re_E)}$

At $O(Re_E)$, $p_{-2}^{(Re_E)}=r^{-2}[A_{-2,0}^{(Re_E)}P_{1,0}+(A_{-2,1}^{(Re_E)}\cos\phi+\hat{A}_{-2,1}^{(Re_E)}\sin\phi)P_{1,1}]$, where the unknown coefficients are obtained as

$$\left.\begin{aligned}
A_{-2,0}^{(Re_E)} &= -\frac{3M(3R-S+3)(R-S)k_2}{35(\lambda+1)^2(3\lambda+2)(4+\lambda)(2+R)^2(3+2R)}\begin{bmatrix}(36\lambda^2+119\lambda+75)E_x^2\\ +(8\lambda^2+42\lambda+40)E_z^2\end{bmatrix}\\
&\quad+\left(\frac{3\lambda+2}{2\lambda+2}\right)U_{dz}^{(Re_E)},\\
A_{-2,1}^{(Re_E)} &= -\frac{3ME_xE_z(3R-S+3)(R-S)(2\lambda^2+63\lambda+45)k_2}{35(\lambda+1)^2(3\lambda+2)(4+\lambda)(2+R)^2(3+2R)}+\left(\frac{3\lambda+2}{2\lambda+2}\right)U_{dx}^{(Re_E)},\\
\hat{A}_{-2,1}^{(Re_E)} &= \left(\frac{3\lambda+2}{2\lambda+2}\right)U_{dy}^{(Re_E)}.
\end{aligned}\right\} \tag{D 1}$$

Appendix E. Expressions for the unknown coefficients of the $O(Ca)$ electric potential

The unknown coefficients present in the $O(Ca)$ electric potential (3.25) are obtained as

$$\left.\begin{aligned}
a_{1,0}^{(Ca)} &= -\frac{9}{5}\frac{(3L_{2,1}^{(Ca)}E_x+2L_{2,0}^{(Ca)}E_z)(R-1)}{(2+R)^2},\\
a_{1,1}^{(Ca)} &= \frac{9}{5}\frac{(L_{2,0}^{(Ca)}E_x-3L_{2,1}^{(Ca)}E_z-6L_{2,2}^{(Ca)}E_x)(R-1)}{(2+R)^2},\quad a_{2,0}^{(Ca)} = -\frac{45}{7}\frac{L_{3,0}^{(Ca)}E_z(R-1)}{(2R^2+7R+6)},\\
a_{2,1}^{(Ca)} &= \frac{15}{7}\frac{(L_{3,0}^{(Ca)}-10L_{3,2}^{(Ca)})E_x(R-1)}{(2R^2+7R+6)},\quad a_{2,2}^{(Ca)} = -\frac{75}{7}\frac{(R-1)L_{3,2}^{(Ca)}E_z}{(2R^2+7R+6)},\\
b_{-2,0}^{(Ca)} &= \frac{3}{5}\frac{(2E_zL_{2,0}^{(Ca)}+3L_{2,1}^{(Ca)}E_x)(R-1)^2}{(R+2)^2},\\
b_{-2,1}^{(Ca)} &= -\frac{3}{5}\frac{(E_xL_{2,0}^{(Ca)}-3L_{2,1}^{(Ca)}E_z-6L_{2,2}^{(Ca)}E_x)(R-1)^2}{(R+2)^2},\quad b_{-3,0}^{(Ca)} = \frac{18}{7}\frac{L_{3,0}^{(Ca)}E_z(R-1)^2}{2R^2+7R+6},\\
b_{-3,1}^{(Ca)} &= -\frac{6}{7}\frac{(L_{3,0}^{(Ca)}-10L_{3,2}^{(Ca)})E_x(R-1)^2}{(2R^2+7R+6)},\quad b_{-3,2}^{(Ca)} = \frac{30}{7}\frac{L_{3,2}^{(Ca)}E_z(R-1)^2}{(2R^2+7R+6)},\\
b_{-4,0}^{(Ca)} &= -\frac{9}{5}\frac{(-L_{2,0}^{(Ca)}E_z+L_{2,1}^{(Ca)}E_x)(R-1)}{(R+2)},\\
b_{-4,1}^{(Ca)} &= \frac{3}{5}\frac{(L_{2,0}^{(Ca)}E_x+2L_{2,1}^{(Ca)}E_z-L_{2,2}^{(Ca)}E_x)(R-1)}{(R+2)},\\
b_{-4,2}^{(Ca)} &= \frac{3}{10}\frac{(L_{2,1}^{(Ca)}E_x+2L_{2,2}^{(Ca)}E_z)(R-1)}{(R+2)},\quad b_{-4,3}^{(Ca)} = \frac{3}{10}\frac{L_{2,2}^{(Ca)}E_x(R-1)}{(R+2)},\\
b_{-5,0}^{(Ca)} &= \frac{12}{7}\frac{L_{3,0}^{(Ca)}E_z(R-1)}{R+2},\quad b_{-5,1}^{(Ca)} = \frac{3}{7}\frac{E_x(L_{3,0}^{(Ca)}-3L_{3,2}^{(Ca)})(R-1)}{(R+2)},\\
b_{-5,2}^{(Ca)} &= \frac{6}{7}\frac{E_zL_{3,2}^{(Ca)}(R-1)}{(R+2)},\quad b_{-5,3}^{(Ca)} = \frac{3}{14}\frac{E_xL_{3,2}^{(Ca)}(R-1)}{R+2}.
\end{aligned}\right\} \tag{E 1}$$

Appendix F. Expressions for the functions $f_1 - f_{10}$ present in the $O(Ca)$ drop velocity

The functions $f_1 - f_{10}$ present in (3.28) are obtained as

$$f_1 = \begin{bmatrix} (-210R^3 - 1155R^2 - 1260 - 2100R)\lambda^4 \\ + (-6215R^2 - 11\,300R - 6780 - 1130R^3)\lambda^3 \\ + (-1480R^3 - 14\,800R - 8880 - 8140R^2)\lambda^2 \\ + (-15\,200R - 9120 - 8360R^2 - 1520R^3)\lambda \\ + (-960R^3 - 9600R - 5760 - 5280R^2) \end{bmatrix}, \tag{F 1a}$$

$$f_2 = \begin{bmatrix} (1260R^3 + 7560 + 12\,600R + 6930R^2)\lambda^4 \\ + (58\,200R + 34\,920 + 32\,010R^2 + 5820R^3)\lambda^3 \\ + (10\,160R^3 + 101\,600R + 55\,880R^2 + 60\,960)\lambda^2 \\ + (46\,080 + 76\,800R + 42\,240R^2 + 7680R^3)\lambda \\ + (11\,440R^2 + 2080R^3 + 20\,800R + 12\,480) \end{bmatrix}, \tag{F 1b}$$

$$f_3 = \begin{bmatrix} (216S - 216R + 81R^2 - 81SR)\lambda^3 \\ + (252S - 1107SR + 1107R^2 - 252R)\lambda^2 \\ + (3618R^2 - 2952S - 3618SR + 2952R)\lambda \\ + (2016R - 1944SR - 2016S + 1944R^2) \end{bmatrix}, \tag{F 1c}$$

$$f_4 = \begin{bmatrix} (432R - 162R^2 - 432S + 162SR)\lambda^3 \\ + (-2214R^2 + 504R - 504S + 2214SR)\lambda^2 \\ + (-7236R^2 + 5904S + 7236SR - 5904R)\lambda \\ + (-4032R - 3888R^2 + 3888SR + 4032S) \end{bmatrix}, \tag{F 1d}$$

$$f_5 = \begin{bmatrix} (2160R - 810R^2 - 2160S + 810SR)\lambda^3 \\ + (-11\,070R^2 - 2520S + 11\,070SR + 2520R)\lambda^2 \\ + (29\,520S - 29\,520R + 36\,180SR - 36\,180R^2)\lambda \\ + (20\,160S - 20\,160R - 19\,440R^2 + 19\,440SR) \end{bmatrix}, \tag{F 2a}$$

$$f_6 = \begin{bmatrix} (960R^3 + 5280R^2 + 9600R + 5760)\lambda^3 \\ + (16\,060R^2 + 17\,520 + 2920R^3 + 29\,200R)\lambda^2 \\ + (14\,400R + 1440R^3 + 8640 + 7920R^2)\lambda \\ + (-5200R - 3120 - 2860R^2 - 520R^3) \end{bmatrix}, \tag{F 2b}$$

$$f_7 = \begin{bmatrix} (-432R - 162RS + 162R^2 + 432S)\lambda^3 \\ + (2214R^2 - 2214RS - 504R + 504S)\lambda^2 \\ + (-7236RS - 5904S + 5904R + 7236R^2)\lambda \\ + (4032R + 3888R^2 - 3888RS - 4032S) \end{bmatrix}, \tag{F 2c}$$

$$f_8 = \begin{bmatrix} (90R^3 + 495R^2 + 540 + 900R)\lambda^4 \\ + (390R^3 + 2340 + 3900R + 2145R^2)\lambda^3 \\ + (340R^3 + 1870R^2 + 3400R + 2040)\lambda^2 \\ + (10\,400R + 5720R^2 + 6240 + 1040R^3)\lambda \\ + (6400R + 640R^3 + 3520R^2 + 3840) \end{bmatrix}, \tag{F 2d}$$

$$f_9 = \begin{bmatrix} (4320R + 1620RS - 1620R^2 - 4320S)\lambda^3 \\ + (-22\,140R^2 + 22\,140RS + 5040R - 5040S)\lambda^2 \\ + (72\,360RS + 59\,040S - 59\,040R - 72\,360R^2)\lambda \\ + (-40\,320R - 38\,880R^2 + 38\,880RS + 40\,320S) \end{bmatrix}, \tag{F 2e}$$

$$f_{10} = \begin{bmatrix} (-900R^3 - 4950R^2 - 5400 - 9000R)\lambda^4 \\ + (-3900R^3 - 23\,400 - 39\,000R - 21450R^2)\lambda^3 \\ + (-3400R^3 - 18\,700R^2 - 34\,000R - 20\,400)\lambda^2 \\ + (-104\,000R - 57\,200R^2 - 62\,400 - 10\,400R^3)\lambda \\ + (-64\,000R - 6400R^3 - 35\,200R^2 - 38\,400) \end{bmatrix}. \tag{F 2f}$$

Appendix G. Expressions for the functions $f_{11} - f_{13}$ present in the steady state transverse position of the drop

The functions $f_{11} - f_{13}$ present in (3.32) and (3.33) are obtained as

$$f_{11} = \left(-\frac{9}{2}\right) \frac{\begin{bmatrix} (2S^2 - 6S + 6R + 6R^2 - 8RS)\lambda^3 \\ + (65S^2 - 260RS + 195R - 195S + 195R^2)\lambda^2 \\ + (-324S + 108S^2 - 432RS + 324R^2 + 324R)\lambda \\ + (135R + 135R^2 + 45S^2 - 135S - 180RS) \end{bmatrix}}{(3 + 2R)(R + 2)^2(198\lambda^5 - 1242\lambda^4 - 7327\lambda^3 - 6292\lambda^2 + 1843\lambda + 2320)}, \tag{G 1}$$

$$\left.\begin{aligned} f_{12} &= \frac{\begin{bmatrix} (-10\,800R^3 - 44\,712R + 39\,258RS - 16\,200 + 66\,312S - 33\,858R^2)\lambda^4 \\ + (-65\,475 - 11\,1591R^2 - 161\,649R - 43\,650R^3 + 133\,416RS + 248\,949S)\lambda^3 \\ + (-40\,419R^2 + 190\,116S - 73\,575 + 64\,944RS - 49\,050R^3 - 92\,016R)\lambda^2 \\ + (-85\,518RS - 15\,525 - 10\,350R^3 + 90\,693R^2 - 58\,977S + 79\,677R)\lambda \\ + (8775 + 56\,700R - 68\,400S + 5850R^3 + 54\,675R^2 - 57\,600RS) \end{bmatrix}}{20(3 + 2R)(R + 2)^2(198\lambda^5 - 1242\lambda^4 - 7327\lambda^3 - 6292\lambda^2 + 1843\lambda + 2320)}, \\ f_{13} &= \left[\frac{105(3\lambda^2 + 5\lambda + 2)(\lambda + 4)(2 + 3\lambda)(\lambda + 1)}{16(-7327\lambda^3 - 1242\lambda^4 + 2320 - 6292\lambda^2 + 1843\lambda + 198\lambda^5)}\right]. \end{aligned}\right\} \tag{G 2}$$

Appendix H. Model validation and grid independence study

First, we validate the numerical code of GERRIS for the particular case of drop motion in Poiseuille flow. We compare the temporal evolution of the transverse position of the drop in figure 18(*a*) with the numerical results obtained by Mortazavi & Tryggvason (2000). Mortazavi & Tryggvason (2000) have employed a front tracking/finite difference method to simulate drop dynamics in a 2D rectangular domain of length $L = 3H$. We use same domain size with periodic boundary conditions along the flow direction. Mortazavi & Tryggvason (2000) have taken the Reynolds number based on channel height ($Re_H = \rho_e V_c H/\mu_e$) as unity. To compare the results, we renormalize $x_d(t)$ by the channel height (H). Figure 18(*a*) shows that the GERRIS code compares very well with the results of Mortazavi & Tryggvason (2000) for the parameters mentioned in the figure caption. The present numerical solutions are obtained considering a cell size of $H/8$ in the bulk fluid and a cell size of $H/256$

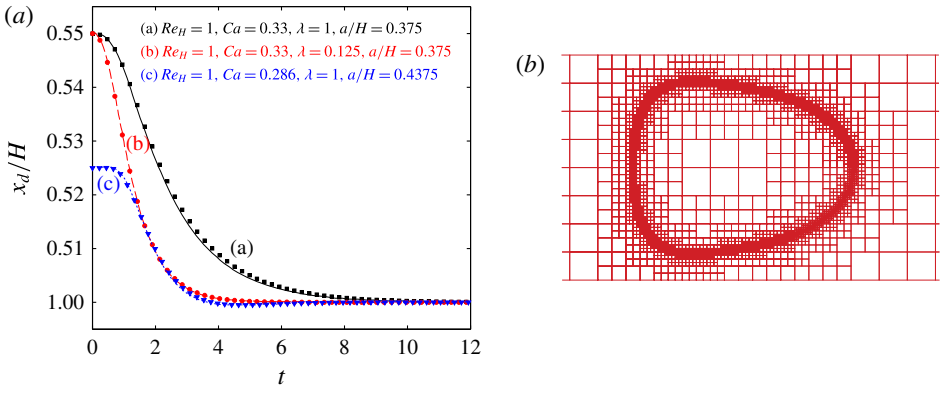

FIGURE 18. (Colour online) (*a*) Temporal evolution of the transverse position of the drop. The transverse position is normalized by channel height H for comparison. Markers represent numerical results of Mortazavi & Tryggvason (2000), while the lines represent the present numerical simulations. (*b*) Structure of the adaptive mesh at time $t = 10$.

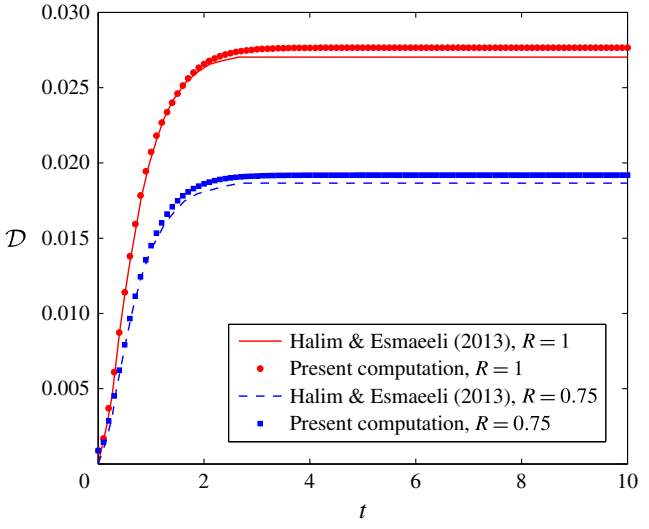

FIGURE 19. (Colour online) Temporal evolution of the Taylor deformation parameter for $R = 0.75$ and $R = 1$. Other parameters have the following values: $Ca = 0.25$, $Re_E = 0.01$, $S = 0.5$, $\lambda = 1$, $Re = 1$, $L = H = 5$, and $\rho_r = 0.5$ (where ρ_r is the density ratio). Present numerical solutions are obtained considering a cell size of $H/8$ in the bulk fluid and a cell size of $H/256$ near the drop interface.

near the drop interface. In figure 18(*b*) we show the structure of the gradient-based adaptive mesh near the drop.

Second, we validate the numerical code of GERRIS for the particular case of drop deformation in a uniform electric field. We compare the temporal evolution of the Taylor deformation parameter in figure 19 with existing numerical results (Halim & Esmaeeli 2013). The Taylor deformation parameter is defined as $D = (L_\parallel - L_\perp)/(L_\parallel + L_\perp)$, where $L_\parallel$ and $L_\perp$ are the length of drop in the parallel and perpendicular directions of the applied electric field. Halim & Esmaeeli (2013)

have employed a front tracking/finite difference method to simulate drop electro-deformation in a 2D rectangular domain of size $L = H = 5$. Figure 19 shows that the GERRIS code compares very well with the results of Halim & Esmaeeli (2013) for the parameters mentioned in the figure caption. However, we obtain a slightly larger deformation, which is due to the consideration of charge convection in the present model. Halim & Esmaeeli (2013) have neglected the charge convection. Feng (1999) has established that charge convection leads to larger deformation of a prolate drop ($D > 0$).

We employ two different grid sizes to investigate the effect of grid resolution in the combined presence of a tilted electric field and Poiseuille flow for $Re_E = Ca = 0.2$, $Re = 0.1$, $R = 1.25$, $S = 1$, $\lambda = 0.1$ and $H = 4$. For both the grids, the cell size in the bulk fluid is taken as $H/8$, while the cell size near the drop interface is taken as $H/128$ and $H/256$ for the two different grids. The drop is released from $x_{d,0} = 1.9$ for both the grids. The final steady state transverse position is obtained as $x_{d,\infty} = 1.939$ for $H/128$ and $x_{d,\infty} = 1.941$ for $H/256$. Previously, López-Herrera *et al.* (2011) have shown that calculations of the electric potential and electric forces are accurately obtained for 51.2 computational cells over the drop radius. So, grid resolution of $H/256$ near the drop which gives 64 computational cells over the drop radius is sufficient to capture the electrohydrodynamics.

REFERENCES

AHN, K., KERBAGE, C., HUNT, T. P., WESTERVELT, R. M., LINK, D. R. & WEITZ, D. A. 2006 Dielectrophoretic manipulation of drops for high-speed microfluidic sorting devices. *Appl. Phys. Lett.* **88** (2), 024104.

BANDOPADHYAY, A., MANDAL, S., KISHORE, N. K. & CHAKRABORTY, S. 2016 Uniform electric-field-induced lateral migration of a sedimenting drop. *J. Fluid Mech.* **792**, 553–589.

BAROUD, C., DELVILLE, J.-P., GALLAIRE, F. & WUNENBURGER, R. 2007 Thermocapillary valve for droplet production and sorting. *Phys. Rev.* E **75** (4), 046302.

BASU, A. S. & GIANCHANDANI, Y. B. 2008 Virtual microfluidic traps, filters, channels and pumps using Marangoni flows. *J. Micromech. Microengng* **18** (11), 115031.

BHAGAT, A. A. S., BOW, H., HOU, H. W., TAN, S. J., HAN, J. & LIM, C. T. 2010 Microfluidics for cell separation. *Med. Biol. Engng Comput.* **48** (10), 999–1014.

BRENNER, H. 1964 The Stokes resistance of a slightly deformed sphere. *Chem. Engng Sci.* **19** (8), 519–539.

BRINGER, M. R., GERDTS, C. J., SONG, H., TICE, J. D. & ISMAGILOV, R. F. 2004 Microfluidic systems for chemical kinetics that rely on chaotic mixing in droplets. *Phil. Trans.* A **362** (1818), 1087–1104.

CASADEVALL I SOLVAS, X. & DEMELLO, A. 2011 Droplet microfluidics: recent developments and future applications. *Chem. Commun.* **47** (7), 1936–1942.

CHAFFEY, C. E., BRENNER, H. & MASON, S. G. 1965 Particle motions in sheared suspensions. *Rheol. Acta* **4** (1), 64–72.

CHAN, P. C.-H. & LEAL, L. G. 1979 The motion of a deformable drop in a second-order fluid. *J. Fluid Mech.* **92** (01), 131–170.

CHAUDHURY, K., MANDAL, S. & CHAKRABORTY, S. 2016 Droplet migration characteristics in confined oscillatory microflows. *Phys. Rev.* E **93** (2), 023106.

CHEN, X., SONG, Y., LI, D. & HU, G. 2015 Deformation and interaction of droplet pairs in a microchannel under ac electric fields. *Phys. Rev. Appl.* **4** (2), 024005.

CHEN, X., XUE, C., ZHANG, L., HU, G., JIANG, X. & SUN, J. 2014 Inertial migration of deformable droplets in a microchannel. *Phys. Fluids* **26** (11), 112003.

CIMPEANU, R., PAPAGEORGIOU, D. T. & PETROPOULOS, P. G. 2014 On the control and suppression of the Rayleigh–Taylor instability using electric fields. *Phys. Fluids* **26** (2).

DAS, D. & SAINTILLAN, D. 2016 A nonlinear small-deformation theory for transient droplet electrohydrodynamics. arXiv:1605.04036v2 [physics.flu-dyn].

DATTA, S., DAS, A. K. & DAS, P. K. 2015 Uphill movement of sessile droplets by electrostatic actuation. *Langmuir* **31** (37), 10190–10197.

DESHMUKH, S. D. & THAOKAR, R. M. 2013 Deformation and breakup of a leaky dielectric drop in a quadrupole electric field. *J. Fluid Mech.* **731**, 713–733.

DING, X., LI, P., LIN, S.-C. S., STRATTON, Z. S., NAMA, N., GUO, F., SLOTCAVAGE, D., MAO, X., SHI, J., COSTANZO, F. & HUANG, T. J. 2013 Surface acoustic wave microfluidics. *Lab on a Chip* **13** (18), 3626–3649.

ESMAEELI, A. 2016 Dielectrophoretic- and electrohydrodynamic-driven translational motion of a liquid column in transverse electric fields. *Phys. Fluids* **28**, 073306.

FENG, J. Q. 1999 Electrohydrodynamic behaviour of a drop subjected to a steady uniform electric field at finite electric Reynolds number. *Proc. R. Soc. Lond.* A **455** (1986), 2245–2269.

FENG, J. Q. & SCOTT, T. C. 2006 A computational analysis of electrohydrodynamics of a leaky dielectric drop in an electric field. *J. Fluid Mech.* **311**, 289.

FERNÁNDEZ, A. 2008 Response of an emulsion of leaky dielectric drops immersed in a simple shear flow: drops less conductive than the suspending fluid. *Phys. Fluids* **20** (4), 043304.

FERNÁNDEZ, A. 2009 Shear flow of an emulsion of drops less conductive than the suspending fluid immersed in an electric field by numerical simulation. *Colloids Surf.* A **338** (1–3), 68–79.

FERRERA, C., LÓPEZ-HERRERA, J. M., HERRADA, M. A., MONTANERO, J. M. & ACERO, A. J. 2013 Dynamical behavior of electrified pendant drops. *Phys. Fluids* **25** (1), 012104.

FRANKE, T., ABATE, A. R., WEITZ, D. A. & WIXFORTH, A. 2009 Surface acoustic wave (SAW) directed droplet flow in microfluidics for PDMS devices. *Lab on a Chip* **9** (18), 2625–2627.

GRIGGS, A. J., ZINCHENKO, A. Z. & DAVIS, R. H. 2007 Low-Reynolds-number motion of a deformable drop between two parallel plane walls. *Intl J. Multiphase Flow* **33** (2), 182–206.

GUO, M. T., ROTEM, A., HEYMAN, J. A. & WEITZ, D. A. 2012 Droplet microfluidics for high-throughput biological assays. *Lab on a Chip* **12** (12), 2146–2155.

HA, J.-W. & YANG, S.-M. 2000*a* Deformation and breakup of Newtonian and non-Newtonian conducting drops in an electric field. *J. Fluid Mech.* **405**, 131–156.

HA, J.-W. & YANG, S.-M. 2000*b* Rheological responses of oil-in-oil emulsions in an electric field. *J. Rheol.* **44** (2), 235.

HABER, S. & HETSRONI, G. 1971 The dynamics of a deformable drop suspended in an unbounded Stokes flow. *J. Fluid Mech.* **49** (02), 257–277.

HALIM, M. A. & ESMAEELI, A. 2013 Computational studies on the transient electrohydrodynamics of a liquid drop. *Fluid Dyn. Mater. Process.* **9** (4), 435–460.

HANNA, J. A. & VLAHOVSKA, P. M. 2010 Surfactant-induced migration of a spherical drop in Stokes flow. *Phys. Fluids* **22** (1), 013102.

HAPPEL, J. & BRENNER, H. 1981 *Low Reynolds Number Hydrodynamics*. Springer.

HETSRONI, G. & HABER, S. 1970 The flow in and around a droplet or bubble submerged in an unbound arbitrary velocity field. *Rheol. Acta* **9** (4), 488–496.

IM, D. J. & KANG, I. S. 2003 Electrohydrodynamics of a drop under nonaxisymmetric electric fields. *J. Colloid Interface Sci.* **266** (1), 127–140.

KARNIS, A. & MASON, S. 1967 Particle motions in sheared suspensions. *J. Colloid Interface Sci.* **24** (2), 164–169.

KHALILI, H. & MORTAZAVI, S. 2012 Numerical simulation of buoyant drops suspended in Poiseuille flow at nonzero Reynolds numbers. *Acta Mechanica* **224** (2), 269–286.

KIM, S. & KARRILA, S. 1991 *Microhydrodynamics: Principles and Selected Applications*. Butterworth-Heinemann.

LAC, E. & HOMSY, G. M. 2007 Axisymmetric deformation and stability of a viscous drop in a steady electric field. *J. Fluid Mech.* **590**, 239–264.

LAMB, H. 1975 *Hydrodynamics*, 6th edn. Cambridge University Press.

LANAUZE, J. A., WALKER, L. M. & KHAIR, A. S. 2013 The influence of inertia and charge relaxation on electrohydrodynamic drop deformation. *Phys. Fluids* **25** (11), 112101.

LANAUZE, J. A., WALKER, L. M. & KHAIR, A. S. 2015 Nonlinear electrohydrodynamics of slightly deformed oblate drops. *J. Fluid Mech.* **774**, 245–266.

LEAL, L. G. 1980 Particle motions in a viscous fluid. *Annu. Rev. Fluid Mech.* **12** (1), 435–476.

LEAL, L. G. 2007 *Advanced Transport Phenomena*. Cambridge University Press.

LINK, D. R., GRASLAND-MONGRAIN, E., DURI, A., SARRAZIN, F., CHENG, Z., CRISTOBAL, G., MARQUEZ, M. & WEITZ, D. A. 2006 Electric control of droplets in microfluidic devices. *Angew. Chem. Intl Ed. Engl.* **45** (16), 2556–2560.

LÓPEZ-HERRERA, J. M., GAÑÁN-CALVO, A. M., POPINET, S. & HERRADA, M. A. 2015 Electrokinetic effects in the breakup of electrified jets: a volume-of-fluid numerical study. *Intl J. Multiphase Flow* **71**, 14–22.

LÓPEZ-HERRERA, J. M., POPINET, S. & HERRADA, M. A. 2011 A charge-conservative approach for simulating electrohydrodynamic two-phase flows using volume-of-fluid. *J. Comput. Phys.* **230** (5), 1939–1955.

MAGNAUDET, J. 2003 Small inertial effects on a spherical bubble, drop or particle moving near a wall in a time-dependent linear flow. *J. Fluid Mech.* **485**, 115–142.

MAHLMANN, S. & PAPAGEORGIOU, D. 2009 Numerical study of electric field effects on the deformation of two-dimensional liquid drops in simple shear flow at arbitrary Reynolds number. *J. Fluid Mech.* **626**, 367.

MANDAL, S., BANDOPADHYAY, A. & CHAKRABORTY, S. 2015 Effect of interfacial slip on the cross-stream migration of a drop in an unbounded Poiseuille flow. *Phys. Rev.* E **92** (2), 023002.

MANDAL, S., BANDOPADHYAY, A. & CHAKRABORTY, S. 2016*a* Dielectrophoresis of a surfactant-laden viscous drop. *Phys. Fluids* **28** (6), 062006.

MANDAL, S., BANDOPADHYAY, A. & CHAKRABORTY, S. 2016*b* Effect of surface charge convection and shape deformation on the dielectrophoretic motion of a liquid drop. *Phys. Rev.* E **93** (4), 043127.

MANDAL, S., CHAUDHURY, K. & CHAKRABORTY, S. 2014 Transient dynamics of confined liquid drops in a uniform electric field. *Phys. Rev.* E **89** (5), 053020.

MANDAL, S., GHOSH, U. & CHAKRABORTY, S. 2016 Effect of surfactant on motion and deformation of compound droplets in arbitrary unbounded Stokes flows. *J. Fluid Mech.* **803**, 200–249.

MELCHER, J. R. & TAYLOR, G. I. 1969 Electrohydrodynamics: a review of the role of interfacial shear stresses. *Annu. Rev. Fluid Mech.* **1** (1), 111–146.

MHATRE, S. & THAOKAR, R. M. 2013 Drop motion, deformation, and cyclic motion in a non-uniform electric field in the viscous limit. *Phys. Fluids* **25** (7), 072105.

MORTAZAVI, S. & TRYGGVASON, G. 2000 A numerical study of the motion of drops in Poiseuille flow. Part 1. Lateral migration of one drop. *J. Fluid Mech.* **411**, 325–350.

MUKHERJEE, S. & SARKAR, K. 2013 Effects of matrix viscoelasticity on the lateral migration of a deformable drop in a wall-bounded shear. *J. Fluid Mech.* **727**, 318–345.

MUKHERJEE, S. & SARKAR, K. 2014 Lateral migration of a viscoelastic drop in a Newtonian fluid in a shear flow near a wall. *Phys. Fluids* **26** (10), 103102.

PAK, O. S., FENG, J. & STONE, H. A. 2014 Viscous Marangoni migration of a drop in a Poiseuille flow at low surface Péclet numbers. *J. Fluid Mech.* **753**, 535–552.

PAMME, N. 2012 On-chip bioanalysis with magnetic particles. *Curr. Opin. Chem. Biol.* **16** (3–4), 436–443.

POPINET, S. 2003 Gerris: a tree-based adaptive solver for the incompressible Euler equations in complex geometries. *J. Comput. Phys.* **190** (2), 572–600.

POPINET, S. 2009 An accurate adaptive solver for surface-tension-driven interfacial flows. *J. Comput. Phys.* **228** (16), 5838–5866.

SAVILLE, D. A. 1997 Electrohydrodynamics: the Taylor–Melcher leaky dielectric model. *Annu. Rev. Fluid Mech.* **29** (1), 27–64.

SCHWALBE, J. T., PHELAN, F. R. JR., VLAHOVSKA, P. M. & HUDSON, S. D. 2011 Interfacial effects on droplet dynamics in Poiseuille flow. *Soft Matt.* **7** (17), 7797.

SEEMANN, R., BRINKMANN, M., PFOHL, T. & HERMINGHAUS, S. 2012 Droplet based microfluidics. *Rep. Prog. Phys.* **75** (1), 016601.

STAN, C. A., GUGLIELMINI, L., ELLERBEE, A. K., CAVIEZEL, D., STONE, H. A. & WHITESIDES, G. M. 2011 Sheathless hydrodynamic positioning of buoyant drops and bubbles inside microchannels. *Phys. Rev.* E **84** (3), 036302.

SUPEENE, G., KOCH, C. R. & BHATTACHARJEE, S. 2008 Deformation of a droplet in an electric field: nonlinear transient response in perfect and leaky dielectric media. *J. Colloid Interface Sci.* **318** (2), 463–476.

TAYLOR, G. 1966 Studies in electrohydrodynamics. I: the circulation produced in a drop by electrical field. *Proc. R. Soc. Lond.* A **291** (1425), 159–166.

TEH, S.-Y., LIN, R., HUNG, L.-H. & LEE, A. P. 2008 Droplet microfluidics. *Lab on a Chip* **8** (2), 198–220.

THAOKAR, R. M. 2012 Dielectrophoresis and deformation of a liquid drop in a non-uniform, axisymmetric AC electric field. *Eur. Phys. J.* E **35** (8), 76.

TORZA, S., COX, R. G. & MASON, S. G. 1971 Electrohydrodynamic deformation and burst of liquid drops. *Phil. Trans. R. Soc. Lond.* A **269** (1198), 295–319.

UIJTTEWAAL, W. S. J. & NIJHOF, E. J. 1995 The motion of a droplet subjected to linear shear flow including the presence of a plane wall. *J. Fluid Mech.* **302**, 45.

UIJTTEWAAL, W. S. J., NIJHOF, E.-J. & HEETHAAR, R. M. 1993 Droplet migration, deformation, and orientation in the presence of a plane wall: a numerical study compared with analytical theories. *Phys. Fluids* A **5** (4), 819.

VIZIKA, O. & SAVILLE, D. A. 2006 The electrohydrodynamic deformation of drops suspended in liquids in steady and oscillatory electric fields. *J. Fluid Mech.* **239** (–1), 1.

VLAHOVSKA, P. M. 2011 On the rheology of a dilute emulsion in a uniform electric field. *J. Fluid Mech.* **670**, 481–503.

WANG, Y. & DIMITRAKOPOULOS, P. 2011 Low-Reynolds-number droplet motion in a square microfluidic channel. *Theor. Comput. Fluid Dyn.* **26** (1–4), 361–379.

WOHL, P. R. & RUBINOW, S. I. 1974 The transverse force on a drop in an unbounded parabolic flow. *J. Fluid Mech.* **62** (01), 185–207.

XU, X. & HOMSY, G. M. 2006 The settling velocity and shape distortion of drops in a uniform electric field. *J. Fluid Mech.* **564**, 395.

YARIV, E. & ALMOG, Y. 2016 The effect of surface-charge convection on the settling velocity of spherical drops in a uniform electric field. *J. Fluid Mech.* **797**, 536–548.

ZHENG, B., TICE, J. D. & ISMAGILOV, R. F. 2004 Formation of droplets of alternating composition in microfluidic channels and applications to indexing of concentrations in droplet-based assays. *Anal. Chem.* **76** (17), 4977–4982.

ZHU, Y. & FANG, Q. 2013 Analytical detection techniques for droplet microfluidics – a review. *Anal. Chim. Acta* **787**, 24–35.

ZHU, Y., ZHU, L.-N., GUO, R., CUI, H.-J., YE, S. & FANG, Q. 2014 Nanoliter-scale protein crystallization and screening with a microfluidic droplet robot. *Sci. Rep.* **4**, 5046.